SAND2014-18114T

SYNTHESIS AND CHARACTERIZATION OF A MATRIX-FREE NANOCOMPOSITE

BY

JESSICA A BIERNER, B.S.

A dissertation submitted to the Graduate School

in partial fulfillment of the requirements

for the degree

Masters of Science

Major Subject: Inorganic Chemistry

New Mexico State University

Las Cruces, New Mexico

September, 2014

“Synthesis and Characterization of a Matrix-Free Nanocomposite”, a thesis prepared by Jessica A. Bierner in partial fulfillment of the requirements for the degree, Master of Science, has been approved and accepted by the following:

William Quintana

Dean of Graduate School

Michael D. Johnson

Chair of the Examining Committee

Date

Committee in charge:

Dr. Michael D. Johnson, Chair

Dr. David Smith

Dr. Michael Englehardt

Dr. Dale L. Huber

DEDICATION

I would like to dedicate this thesis to my selfless and amazing husband, Matt and my precious children, Addison and Matthew II, who make my life incredible each and every day. Without their hard work and sacrifice this work would not have been possible. With every late night and missed weekend activity they allowed me to reach beyond myself and achieve my goal. I appreciate them more than I could ever put into words and my biggest hope is to use this achievement to better their lives into the future.

ACKNOWLEDGMENTS

I owe an incredible deal to my research advisor at Sandia National Laboratories, Dr. Dale Huber. It is his insight, experience, and forward thinking that made this research project possible. I am so very grateful for the many hours of hard work and late nights he invested not only in the research that was done, but in believing in me and my training as a scientist. His ability to teach and mentor allowed me to become confident in the scientist that I have become and for that I will be forever grateful.

I would also like to thank my advisor at New Mexico State University Dr. Michael Johnson, the Chairperson of my dissertation committee and the first advisor I had when starting college as a freshman. It was he who convinced me the world wasn't over when I took and failed my entrance exam into higher math classes and him who allowed me into his lab as a Master's student to continue my education to the next level. He has provided years of support and guidance in my scientific learning and I will always be grateful.

I would also like to give a great thanks to my lab mates at Sandia whose assistance and willingness to give of their time and effort to help me both with understanding of science concepts and in lab work allowed me to reach this goal. I am truly appreciative of all of their contributions.

I need to say thanks to my manager, Kate Bogart and my Lab Lead and supervisor, Henry Peebles, for giving me the time, the guidance and the insights to do this research while working a full-time job. Through all the hard

work, I knew that these two believed in me and my ability to succeed. I am grateful I was hired into the position I was, where I encountered this kind of support. I hope to make them proud with the scientist I am turning out to be.

Lastly to mention, but first in my heart are my family and friends. Without their continuous support and encouragement, my optimism through this project would have long been used up. Through the numerous hours of baby-sitting and the heartening conversations when I felt discouraged, I always knew that my family and friends were behind me 110%. My love for them flows deep and true and I will always say that this degree belongs to all of us.

The body of research described in this dissertation was supported by the U.S. Department of Energy, Office of Basic Energy Sciences, Division of Materials Science and Engineering. HRTEM imaging and XRD/SAXS measurements were performed courtesy of the Center for Integrated Nanotechnologies, a U.S. Department of Energy, Office of Basic Energy Sciences user facility. Sandia National Laboratories is a multi-program laboratory managed and operated by Sandia Corporation, a wholly owned subsidiary of Lockheed Martin Corporation, for the U.S. Department of Energy's National Nuclear Security Administration under Contract DE-AC04-94AL85000.

VITA

[redacted]

2005	Graduated from Belen High School Belen, New Mexico
2009	Graduated from New Mexico State University with B.S in Chemistry, Las Cruces, New Mexico
2009-2011	Teaching Assistant, Department of Chemistry, New Mexico State University
2011-Present	Senior Technologist, Sandia National Laboratories Albuquerque, New Mexico

Professional and Honorary Societies

American Chemical Society

Publications [or Papers Presented]

J. J. Scepaniak, J. A. Young, R. P. Bontchev, and J. M. Smith, **(2009)** *Formation of Ammonia from an Iron Nitrido Complex*, Angewandte Chemie International Edition, 48(17): 3158-3160

J. A. Young, **(2009)** *Investigation into the Mechanism of Hydrogen Atom Transfer to an Iron Nitrido Complex*, Undergraduate Research Creative Arts Symposium, NMSU

J. A. Young, **(2009)** *Investigation into the Mechanism of Hydrogen Transfer to An Iron Nitrido Complex* [Undergraduate Honors Thesis], Las Cruces, NM: New Mexico State University.

Field of Study

Major Field: Inorganic Chemistry

SYNTHESIS AND CHARACTERIZATION OF A MATRIX-FREE NANOCOMPOSITE

BY

JESSICA A. BIERNER, B.S

Master of Science

New Mexico State University

Las Cruces, New Mexico, 2014

Dr. Michael D. Johnson, Chair

Iron nanoparticles have a number of magnetic properties that make them a potentially useful material for transformer applications. These desirable traits include high saturation magnetization, high susceptibility, and very low magnetic hysteresis. Before iron nanoparticles can even be tested for applicability, however, a number of scientific hurdles must be overcome. First an affordable and scalable synthetic approach must be developed, and the results of these large scale reactions must be fashioned

into a solid material. To be of use, this solid material must have very high loading of iron nanoparticles and must be relatively easy to form into desired shapes.

To achieve these goals, iron nanoparticles were synthesized by the thermal decomposition of iron pentacarbonyl in the presence of dodecylamine which bound to the surface of the particles. This reaction was scaled up to a multi-gram scale with only minor changes in size and shape control. These particles were then fashioned into “matrix-free nanocomposites”, where the particles were cross-linked to each other. This was achieved by first exchanging the surface coating for a combination of hexylamine and 1,6-diaminohexane. The diamine provided primary amines on the particle surface that were available for further reaction. These were shown to be capable of reacting with a triepoxide cross-linker to form a hard, solid material, analogous to the cure of a common epoxy adhesive. Loading of up to 80% iron by mass (about 43% by volume) was achieved.

The magnetic properties of these matrix-free nanocomposites were characterized to determine to what degree they were altered during the transformation into nanocomposites. The changes were minor and included a modest increase in the blocking temperature (the ferromagnetic to superparamagnetic transition temperature). The high magnetization and susceptibility, as well as the low magnetic hysteresis were intact. The nanocomposites produced appear to be excellent candidate materials for

transformer cores. Considerable engineering issues are still outstanding, including additional scale-up, molding of large parts, and reaction optimizations. Despite these outstanding issues, the chemistry has been developed and confirmed, and the concept proven on a scale larger than is typical in the chemical literature.

TABLE OF CONTENTS

LIST OF TABLES AND SCHEMES

LIST OF FIGURES

SYMBOLS AND ABBREVIATIONS

Symbol	Unit	Property
E_a	kJ/mol	Activation energy
κ	numerical	Anisotropy constant
k_B	numerical	Boltzmann constant
ρ	g/mL	Density
f	Hz, kHz	Frequency
L	cm, mm, μm, nm	Length; centimeter, millimeter, micrometer, and nanometer
H	A/m	Magnetic field (strength), sometimes given as $\mu_0 H$ in tesla (T)
m	μ_B, $A \cdot m^2$	Magnetic moment
m	mg, g	Mass, milligram and gram
M	A/m, G	Magnetization per unit volume
σ	$A \cdot m^2/kg$	Magnetization per unit mass
σ_{sat}	$A \cdot m^2/kg$	Saturation magnetization per unit mass
K_1	$J \cdot m^{-3}$	Magnetocrystalline anisotropy constant

Symbol	Unit	Property
t	s, min, h	Time
τ_0	s	Attempt time
τ_B	s	Brownian relaxation time
τ_N	s	Néel relaxation time
T	K, °C	Temperature (K)
T_B	K, ºC	Blocking temperature
T_C	K, ºC	Curie temperature
T_N	K, ºC	Néel temperature
V	µL, mL, L	Volume; microliter, milliliter, and liter

Abbreviation	Meaning
3D	Three dimensional
α-Fe	Alpha iron, ferrite
α-Fe_2O_3	Hematite
AC	Alternating current
ASTM	American Society for Testing and Materials
bcc	Body-centered cubic

Abbreviation	Meaning
b.p.	Boiling point
$C_{15}H_{19}NO_4$	N,N-Digylcidyl-4-glycidoxyaniline
CO	Carbon monoxide
Co	Cobalt
δ-Fe	Delta iron
DC	Direct current
DDSA	2-Dodecenylsuccinic anhydride
DOE	Dioctyl ether
DPM-30	2,4,6-Tris(dimethylaminomethyl)phenol, an accelerator
DSC	Differential scanning calorimetry
ε-Fe	Epsilon iron, hexaferrum
fcc	Face-centered cubic
FC	Field cooled
Fe	Iron
$Fe(CO)_5$	Pentacarbonyliron(0), commonly referred to as iron pentacarbonyl
Fe_3O_4	Magnetite

Abbreviation	Meaning
ɣ-Fe	Gamma iron, austenite
ɣ-Fe_2O_3	Maghemite
GATR	Grazing angle attenuated total reflectance
HRTEM	High resolution transmission electron microscopy
IR	Infrared
LPT	Large power transformer
N_2	Nitrogen
Ni	Nickel
NMA	Methyl-5-norbornene-2,3-dicarboxylic anhydride or methylnadic anhydride
rpm	Revolutions per minute
r.b.	Round bottom flask
SAXS	Small angle X-ray scattering
SQUID	Superconducting quantum interference device
TGA	Thermogravimetric analysis
THF	Tetrahydrofuran
TEM	Transmission electron microscopy
UV	Ultra violet

Abbreviation	Meaning
UV-Vis	Ultra violet- visible range of the light spectrum
XRD	X-ray diffraction
ZFC	Zero field cooled

CHAPTER 1- INTRODUCTION

1.1 Material Selection for High Susceptibility Transformer Cores

1.1.1 Transformer Core Introduction

The United States represents approximately 20 percent of the global market in consumption of power transformers as of 2010.[1] This market has a value estimated at over $1 billion USD. The United States also has the largest electrical infrastructure in the world with the largest installed base of Large Power Transformers (LPTs). While the actual total number of LPTs installed in the United States is not easy to estimate, it is commonly thought to be in the range of tens of thousands of transformers.[1-4]

Key drivers for future transformer market development include: an increase in electricity demand in developing countries, replacement of old electric power equipment in matured economies, a boost for high voltage power transformers, and capital expenditure in the power sector worldwide.[5] In addition, the adoption of energy efficiency standards in developed markets, such as Europe and the United States, as well as in emerging markets, such as China and India, are expected to create demand for new, more efficient electricity equipment, including power transformers.[5]

In order to make transformer cores more efficient, it is beneficial to address the two main forms of magnetizing current loss: hysteresis losses and eddy current loss. Hysteresis is the phenomenon that occurs when a ferromagnetic

material is magnetized in one direction, and does not relax back to zero magnetization when the imposed magnetizing field is removed. The material must be driven back to zero by a field in the opposite direction causing the material to trace out a loop called a hysteresis loop as shown in Figures 1.1 and 1.2. This loop represents the lack of retraceability of the magnetization curve, and it is related to the existence of magnetic domains in the material. Once the magnetic domains are reoriented, it requires energy input to turn them back again.

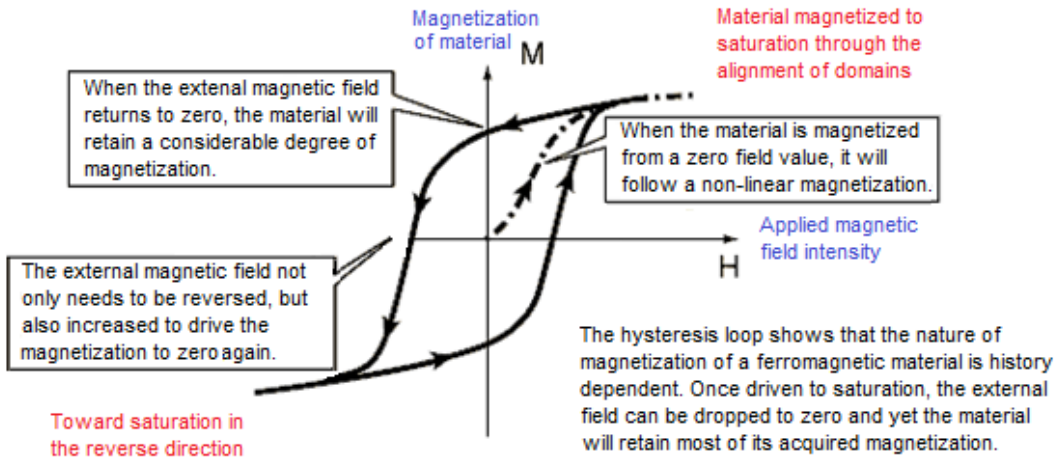

Figure 1.1: Hysteresis Loop Diagram.

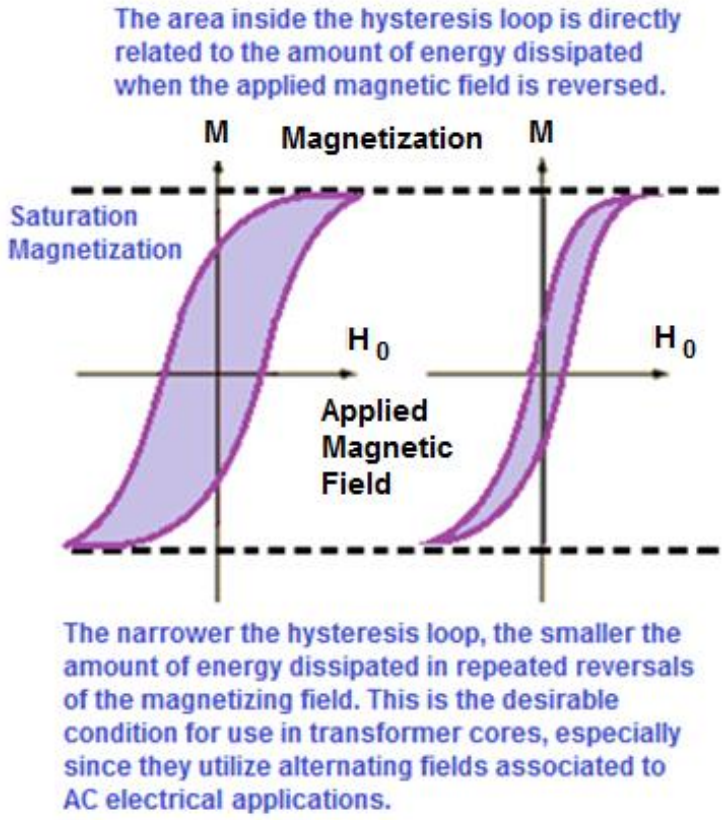

Figure 1.2: Variations in Hysteresis Curves.

Eddy current losses (Figure 1.3) occur when a magnetic field and a conducting material move relative to each other. In the case of an AC transformer, the field is oscillating and the transformer core is stationary. Eddy currents induce currents secondary, or perpendicular, to the primary function of the transformer. The power generated is dissipated in the form of heat and is therefore an energy loss. This phenomenon is dependent on the material selected for use in the core and not dependent on any other property of the transformer core.[6]

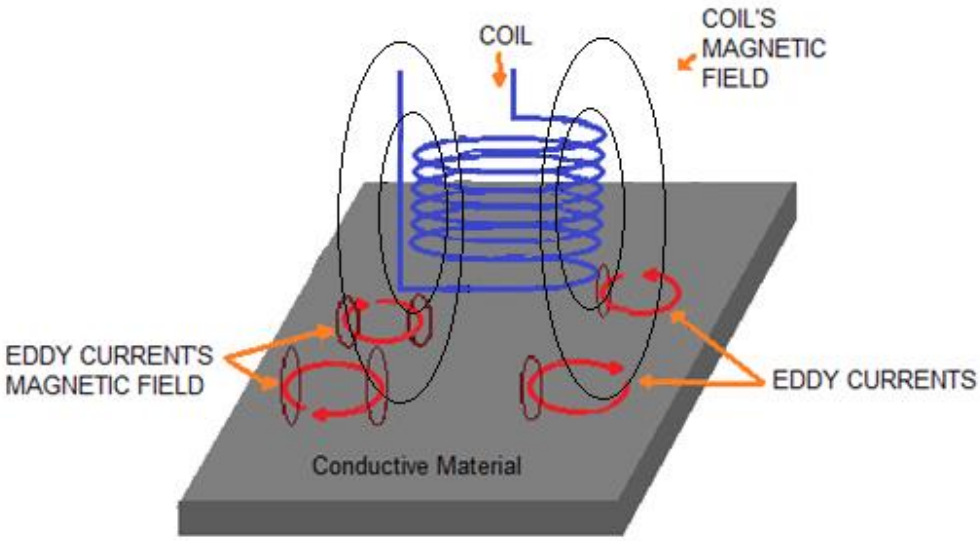

Figure 1.3: Representation of Eddy Current Interactions on a Magnetic Field.

This thesis focuses on the synthesis of a matrix-free nanocomposite to potentially resolve the above issues and create a more efficient transformer core. By using nanoscale magnetic particles, the hysteresis and eddy current losses generated by the material can be greatly diminished or even eliminated.[7, 8] This suggests using a nanoscale magnetic material, which should increase the energy efficiency of the system.

1.1.2 Abundant and Low Cost Material

Iron has been known to mankind for over 5000 years in its pure form.[9] It is the fourth most abundant element by weight in the Earth's crust (comprising 5.6%, Figure 1.4) and is also thought to make up the majority of the Earth's

core.[10] Iron is the most abundant, least expensive and most used of all metals.[11, 12]

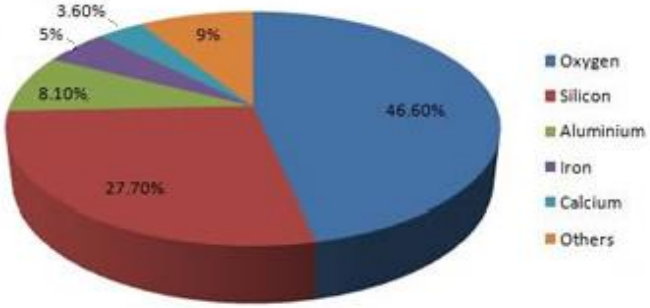

Figure 1.4: Iron's abundance in the Earth's crust.

Three allotropes of iron exist at atmospheric pressure and a fourth allotrope only exists at very high pressures.[13] As molten iron cools, it first crystallizes into a body-centered cubic (bcc) crystal structure around 1500 ºC which is known as delta iron (δ-Fe). As it cools further, to around 1400 ºC, it changes to a face-centered cubic (fcc) crystal structure known as gamma iron (γ-Fe) or austenite. Alpha iron (α-Fe), also known as ferrite, is the most common allotrope of iron at 912 ºC and below, also having a bcc crystal structure. The fourth allotrope of iron is epsilon iron (ε-Fe), or hexaferrum, and is rarely seen due to the high pressure environment needed to sustain it.[13]

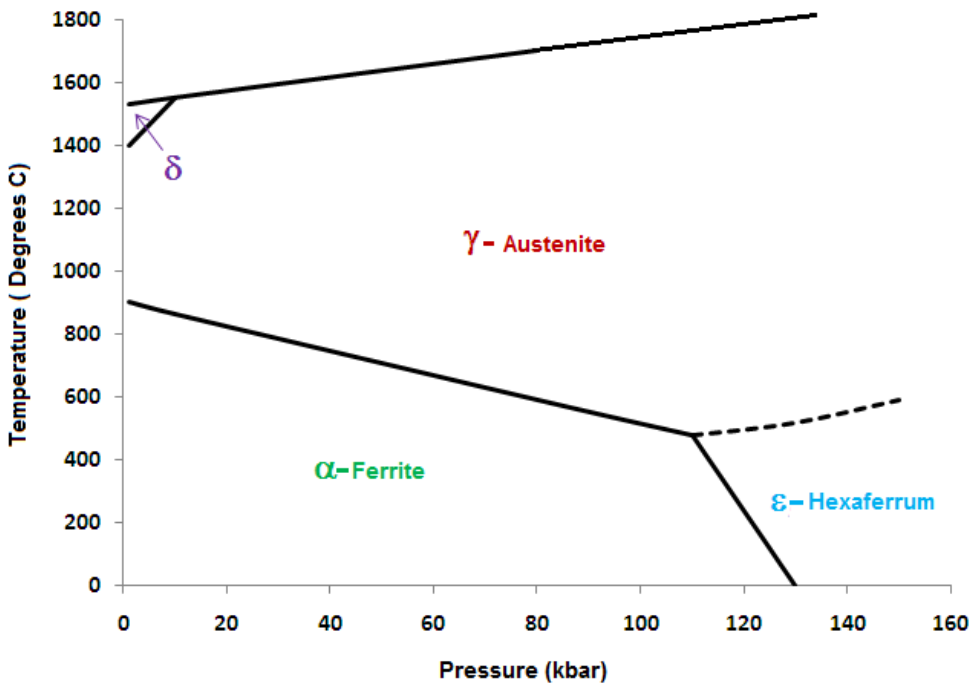

Figure 1.5: The pure iron allotrope phase diagram denoting the different allotropes. α, γ, and ε refer to ferrite, austenite, and hexaferrum respectively. δ-iron is the higher temperature designation of ferrite.

Elemental iron reacts readily with water and oxygen, slowly forming the oxides: hematite (α-Fe_2O_3), maghemite (γ-Fe_2O_3), and magnetite (Fe_3O_4).[14] This reactivity can be troublesome, especially for zero-valent iron (elemental iron without oxidation). Finely divided iron, therefore, is only applicable where air and water can be excluded or in an inert or reducing atmosphere.

From the above discussion of the potential nanoscopic magnetic particles have in transformer core applications, and the abundant and cost-effective nature of iron, the conclusion can be made that investigating iron nanoscopic

particles would be a worthy endeavor. As such, the synthesis, characterization, and encapsulation of zero-valent iron nanoparticles for use in low-loss transformer cores is the main focus of this work. Hence, understanding and overcoming the above challenges was an important part of the research and successful completion of this project.

1.1.3 Nanoparticle Behavior

According to the American Society for Testing and Materials (ASTM) a nanoparticle has lengths in two or three dimensions greater than 0.001 micrometer (1 nanometer) and smaller than about 0.1 micrometer (100 nanometers).[15] These are referred to more generally as ‘particles’, or ‘nanoparticles’. Figure 1.5 shows the relative size of both man-made and natural objects at the nanoscale. The commonly accepted upper limit for nanoparticle size (100 nm) is supported by evidence that below 100 nm, particles behave differently in respect to both chemical and physical properties. Nanoparticles tend to be more reactive since they possess a high amount of energy potential for reaction due to high specific surface area to volume ratios.[12] This is especially true for iron at the nanoscale, where the surface area of the particles enhances the reactivity leading to rapid oxidation in air to the point of being pyrophoric.[16]

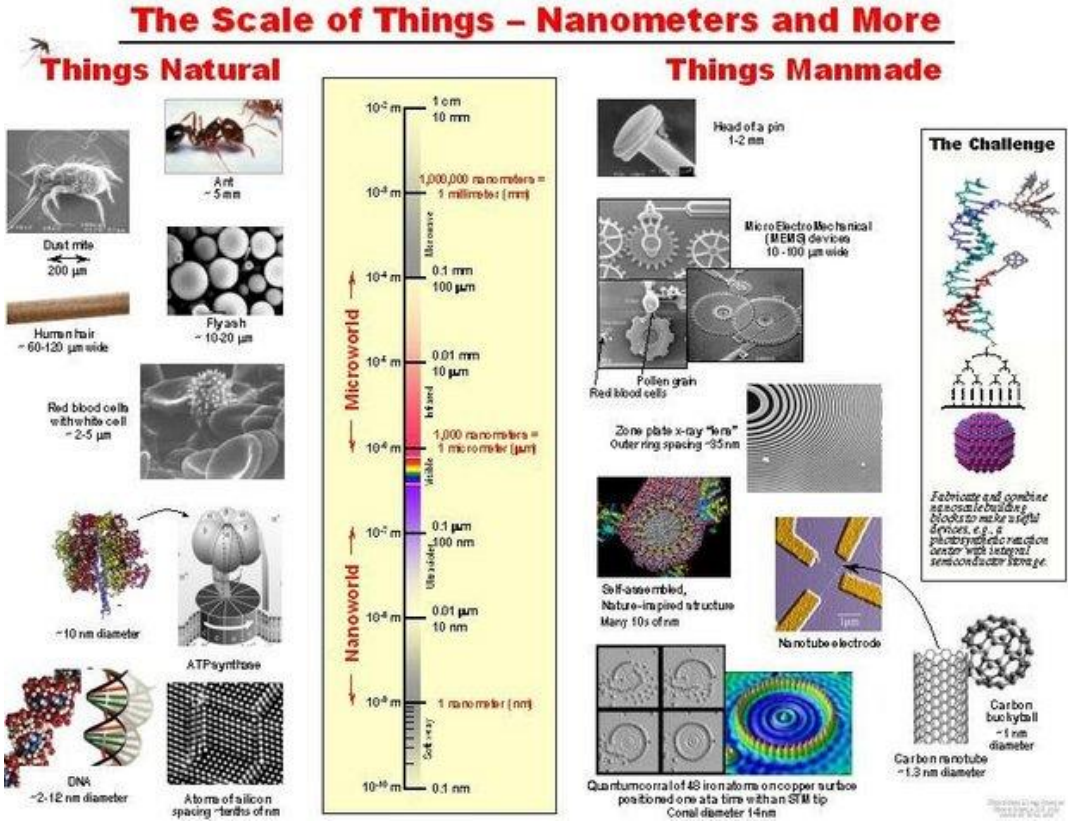

Figure 1.6: Representation of natural and man-made objects at the nanoscale designed by the Office of Basic Energy Sciences (BES) for the U.S. Department of Energy.

Magnetic materials, such as Co, Ni, Fe, and their oxides are commonly used in transformer core applications.[17] Hence, the nanoparticles of these metals are now being explored for transformer core applications due to their highly magnetic nature which far exceeds that of the bulk materials.[18, 19] As mentioned previously, the focus of this work will be iron nanoparticles. In order to fully comprehend the characterization of using this material and why it is advantageous over other materials, an introduction into magnetic

concepts and principles must be made. A few of the critical magnetic properties discussed later in this thesis are defined in the next section.

1.1.4 Magnetic Terminology

Paramagnetic materials have magnetic spins which are not aligned and are randomly oriented in the absence of a magnetic field. Ferromagnetic materials have neighboring spins which are aligned even in the absence of a magnetic field, but may form magnetic domains which have different orientations in the absence of a magnetic field, possibly resulting in net zero magnetization. Antiferromagnetism is displayed when a material has spins aligned antiparallel (180 degrees from each other), exactly cancelling out and resulting in a material with no net magnetic moment either with or without an externally applied field. Ferrimagnetic materials have spins aligned antiparallel but not perfectly cancelling each other, whether due to spins of greater magnitude or more of one orientation than another, which results in behavior similar to ferromagnetism but with lower magnitude since some spins are cancelled out.

A ferromagnetic material is said to have magnetocrystalline anisotropy if it takes more energy to order the magnetic spins in one direction over another. One of the best ways to explain magnetocrystalline anisotropy is to note that the energy it takes to reorder the magnetization of a sample is also referred to as the activation energy. When considering a system with uniaxial anisotropy

(or anisotropy in only one direction), there are two energy minima at opposite spin orientations. These two orientations are separated by an energy barrier known as the activation energy, E_a. For ease of calculations, the minima are aligned on one axis, called the easy axis. When the magnetization vector of a particle is aligned with the easy axis, the magnetic energy is minimized. The energy then increases with the increased angle of tilt away from the easy axis. The difference between the energy at the first minima and the opposite spin orientation is the activation energy, or magnetocrystalline anisotropy (Figure 1.7, adapted from [20]).

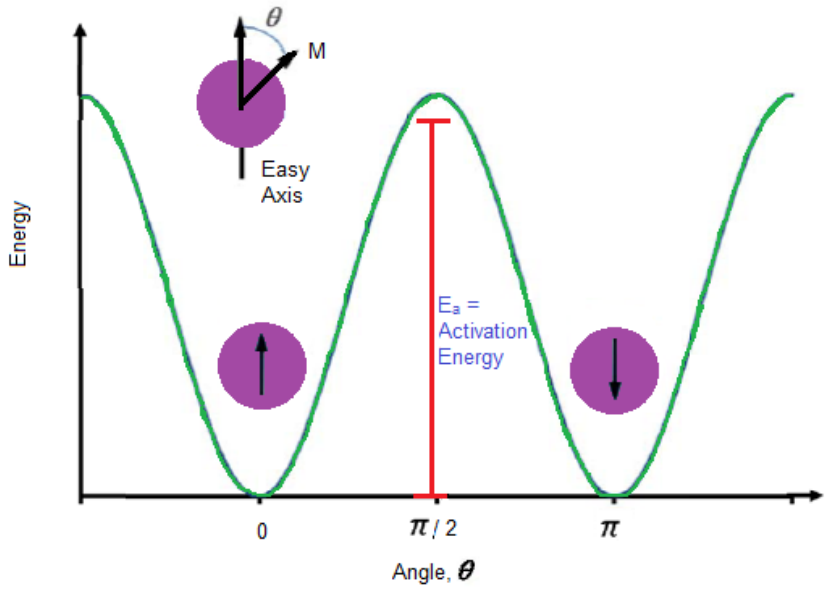

Figure 1.7: The magnetocrystalline anisotropy as a function of magnetic direction. E_a is the energy barrier to reverse the magnetization and θ is the angle of tilt between the vector of magnetization and the easy axis.

It is typical for materials with high magnetocrystalline anisotropy to also have high coercivities (the resistance of a ferromagnetic material to becoming

demagnetized), which makes them permanent magnets, which would be non-ideal for use in transformer core applications.

Saturation magnetization (σ_s) is the value of sample magnetization reached when an increase in an applied external magnetic field, H, cannot increase the magnetization of the material any further as shown in Figure 1.8. The coercive field is where the value of H passes through zero after the external field has been turned off.

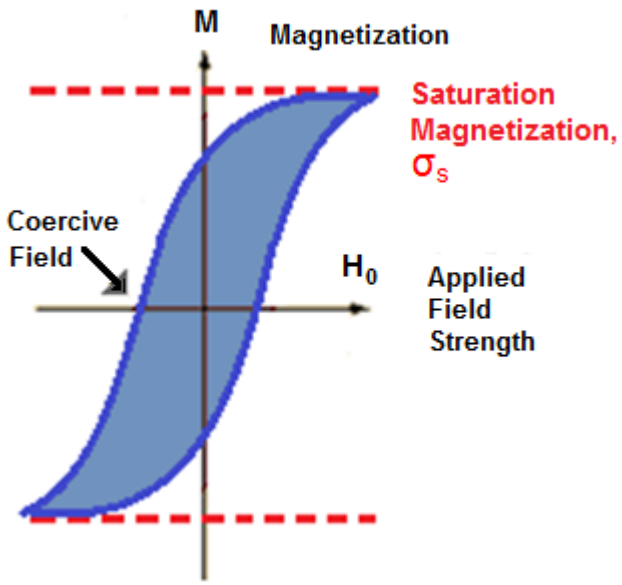

Figure 1.8: Magnetization properties of a material: saturation magnetization, and coercive field representations, where the coercive field is where the value of H falls and passes through zero after the external field has been turned off.

The nanoparticle blocking temperature is the temperature above which particles behave superparamagnetically, which is a special characteristic of

nanoparticles smaller than about 40 nm which will be explained in much greater detail in a following section.

1.1.5 Magnetic Properties of Iron

Magnetic nanoparticles are of great interest today, and iron is among the most useful of magnetic materials.[21] Table 1 shows some of the properties for common ferromagnetic elements, such as iron.

Table 1.1: Properties of the Ferromagnetic Elements

Element	σ_s at 0 K [$A \cdot m^2 \cdot kg^{-1}$]	σ_s at 293 K [$A \cdot m^2 \cdot kg^{-1}$]	*m* (μ_B)	K_1 $J \cdot m^{-3}$	T_c [K]
Fe	222	218	2.22	48	1043
Co	162	161	1.76	410	1388
Ni	57	54	0.61	-5	627

σ_S values are given at both absolute zero and at 0 ºC, *m* is the magnetic moment of the material, K_1 is the magnetocrystalline anisotropy constant, and T_C is the Curie temperature (where the material's ferromagnetism changes to paramagnetism).

Alpha iron has very high saturation magnetization, and relatively low magnetocrystalline anisotropy when compared to other magnetic metals. When iron is oxidized, it forms hematite (α-Fe_2O_3) which is antiferromagnetic as well as maghemite (γ-Fe_2O_3) and magnetite (Fe_3O_4) which are both ferrimagnetic. While the ferrimagnetic oxides have significant saturation magnetizations, they are less than half of the value of iron metal. These oxides are therefore less useful for magnetic transformer coils. For this project, the goal is to synthesize zero-valent iron nanoparticles in order to

take advantage of the higher saturation magnetization, making the exclusion of air and water a crucial experimental factor.

As can be seen in Table 1.1, iron has the highest room-temperature value of σ_s of any element and also has a Curie temperature (T_c) that is high enough for the vast majority of practical applications. The T_c is the temperature above which ferromagnetic ordering is lost. Iron has the further advantage of being a soft magnetic material. Its moldability is important for transformer core applications and makes iron a better candidate for study than cobalt, which has the second-highest room-temperature value for σ_s.

Iron's lower magnetocrystalline anisotropy and higher saturation magnetization in comparison to other, similar, magnetic metals, confirms that iron is an ideal material for use in transformer applications. Furthermore, this project hopes to take advantage of the difference in the magnetic properties of iron as a bulk material versus nanoparticles. Bulk iron is rarely used for transformer applications due to the high eddy current losses that result from bulk iron being a good conductor.[22] Small particles of iron, however, could possibly be suspended in a non-conducting matrix, such as a composite, to suppress eddy current losses. This is currently done commercially with micron scale particles of iron;[23] though these materials still experience significant magnetic losses due to the magnetic hysteresis inherent in bulk iron. To eliminate this loss also, we need to utilize a hysteresis-free magnetic

material. Nanoparticles of appropriately small size can be hysteresis-free; also known as superparamagnetic.[24]

1.2 Superparamagnetism in Iron Nanoparticles

All magnetic particles that are micron sized and larger have multiple magnetic domains in the absence of an external field that are on the order of 10's of nanometers per domain. (The actual size of the magnetic domains in a material is an inherent characteristic of the material itself.) These particles magnetize through the growth of domains in the direction of an applied magnetic field. As they magnetize, the particles begin to form an external magnetic field where none previously existed. The formation of this external field increases the overall energy of the system. This energy cost limits the susceptibility (the slope of the magnetization curve) for multi-domain particles.

Nanoparticles that are below the characteristic size of magnetic domains in an unmagnetized material will always have a single magnetic domain. [21] These particles behave as if they have a single giant spin composed of all of the individual spins in the particle. Because the particle is always fully saturated, it constantly has an external magnetic field, so magnetization of single domain particles now consists simply of orienting the giant spins into the same direction. This process generates a net magnetic moment for the particle ensemble. For individual particles, there is little energy penalty for this magnetization mechanism because the external field of each individual

particle already existed. Therefore, single domain particles have much higher susceptibility than multi-domain particles.[25, 26]

Figure 1.9, below, illustrates how an external field is at a lower energy for smaller particles. Large particles energetically favor domain walls since the external field energy is larger. With a larger external field, the energy needed to create domain walls can be easily spared; while that would not be the case for lower energy external fields of smaller particles.

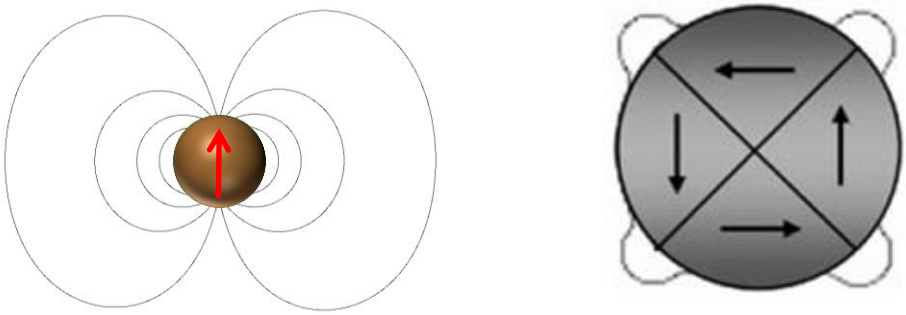

Figure 1.9: The stray magnetic field near spherical particles. Left: The stray field of a single domain particle. Right: Through the creation of domain walls, the stray field of a multi-domain particle is reduced greatly; however energy must be expended in the creation of domain walls.

Single domain particles are superparamagnetic when they possess sufficient thermal energy to freely reorient the direction of their individual magnetic moments. In this state they are easily magnetized, although an ensemble of particles has no net moment in the absence of a magnetic field.[12]

Superparamagnetism is dependent on the size of the particles and their temperature. At high temperatures, the single large spin rotates freely and the

magnetization curve of the material exhibits no hysteresis. This is significant since hysteresis is one of the main energy losses in magnetic materials.[27]

The particle susceptibility is also temperature dependent and passes through a maximum at T_B, the blocking temperature. It then decreases as the temperature continues to increase.[27] T_B is the point below which the thermal energy in the sample is no longer sufficient to overcome the activation energy required to reorient the spins (within the time scale of the experiment). Below this temperature, the particles exhibit hysteresis and are referred to as ferromagnetic.

The rearrangement of the spin of a particle is thermally activated and follows Arrhenius kinetics. The activation energy, E_a, is known as anisotropy energy when speaking in magnetic terms. E_a is proportional to the product of the anisotropy constant, K, and the nanoparticle volume, V as follows:

$$E_a = K \cdot V \tag{1-1}$$

For magnetization applications, Arrhenius kinetics are represented by the Néel-Brown equation:

$$\tau_N = \tau_0 exp\left(\frac{E_a}{k_B T}\right) \tag{1-2}$$

where τ_N is the Néel relaxation time—the time required for a particle's spin to reorient, τ_0 is the attempt time (generally on the order of 10^{-9} sec), k_B is the

Boltzmann constant, and T is the temperature in K. The value of τ_N is extremely sensitive to particle size. For large particles, the energy barrier, E_a, is too large to be surpassed on a typical laboratory time scale (i.e. Néel relaxation times become very long, on the order of days to weeks). In contrast, for smaller particles, the energy required to reorient the spin becomes less than the thermal energy available. This allows the particles to freely reorient their magnetic spins. The predominant behavior depends on the temperature of the system. The critical temperature above which thermal energy allows for random reorientation of the spins can be calculated. This temperature is known as the blocking temperature (T_B) and can be derived from equation 1-2 as the following:

$$T_B = \frac{KV}{ln\left(\frac{\tau}{\tau_0}\right)k_B} \quad (1\text{-}3)$$

Due to its low magnetocrystalline anisotropy (K), iron has a lower T_B than most other nanoparticles of the same size.[28] Equation 1-3 predicts that the T_B of the material is directly dependent on particle volume. This is the motivation for synthesizing smaller nanoparticles; the greater the particle diameter, the higher the blocking temperature will be. In order to keep the blocking temperatures in the practical range for our applications, it is important to synthesize very small nanoparticles under approximately 20 nm in size.[27]

Iron nanoparticles up to about 15 nm in size behave superparamagnetically at room temperature.[27] This, along with their high susceptibility, large saturation magnetization, and low hysteresis and eddy current losses (when appropriately separated from neighboring particles), suggests iron nanoparticles would be an ideal material for use in transformer cores.

1.3 Nanocomposite Design

1.3.1 Definition

In order to take advantage of iron nanoparticles in transformer core applications, it is necessary to suspend the nanoparticles in a matrix, thereby forming a nanocomposite, to keep the particles separate and prevent eddy current losses. The concept of nanocomposites has been around for several years[29, 30] along with potential to create a matrix-free composite with magnetic nanoparticles.[31]

The field of nanocomposites involves the study of multiphase materials where at least one of the constituent phases has one dimension less than 100 nm.[32] The promise of nanocomposites lies in their multi-functionality and the possibility of realizing unique combinations of properties unachievable with traditional, bulk, materials. The challenges include control over the distribution in size and dispersion of the nanosize constituents as well as tailoring and understanding the role of interfaces between structurally or chemically dissimilar phases on bulk properties.[32]

1.3.2 Unique Properties

The main factors that were considered in the design of the nanocomposite system used in this research were the effects of ligand size (for keeping the nanoparticles from agglomerating) and the ability of the ligand to allow the nanoparticles to maintain their superparamagnetic characteristics.

A solution-based synthesis was used to produce the zero-valent iron (Fe^0) nanoparticles for this research. The extreme sensitivity of zero-valent iron nanoparticles to air and water made synthesis difficult. There are numerous reports in the literature of particles that possess an oxide layer or a magnetically dead layer on the surface. [12, 33-35] The synthesis is further complicated by the fact that an oxide layer forms from the interaction of the organic ligands or surfactants used to create the nanoparticles and keep them from agglomerating with the surface of other particles.[27] The transfer of small amounts of oxygen within the organic ligands or surfactants to the surface of the particles forms this oxide layer. These layers significantly lower the magnetization saturation of the particles in comparison to bulk iron, meaning they would have no use for application in transformer cores. A strong tie between how strongly the surfactant interacts with the particle surface and the decrease in the saturation magnetization has been established.[35] A solution to this problem was proposed in the use of a weakly interacting surfactant such that stabilization of the particles to prevent agglomeration could occur

without binding so strongly that the surfactant causes an oxide layer to form causing a decrease in magnetic properties. [27]

1.3.3 "Matrix-Free" Nanocomposites

Recently, a supramolecular building block approach for the preparation of a new family of nanocomposites (comprised of nanoparticles cross-linked by polymer bridges that do not require a polymer matrix) has been investigated.[31] These "matrix-free" nanocomposites are not prone to the nanoparticle aggregation effects that plague conventional nanocomposites. They hold promise to provide exceptionally high strength and toughness due to the formation of covalent bridges linking the nanoparticles into a matrix-free composite.[31] High strength and toughness are desirable properties to have in a longer lasting, more efficient material for use in transformer cores.

Figure 1.10 shows the difference between the settling and dispersion issues that arise when using fillers in commercial epoxy systems which are currently available today and the ideal matrix-free composite system proposed for this work. By crosslinking nanoparticles together through the reactivity of the ligands attached to the particle surfaces, a uniform dispersion of particles becomes an inherent part of the nanocomposite itself, removing the difficulties with settling while curing.

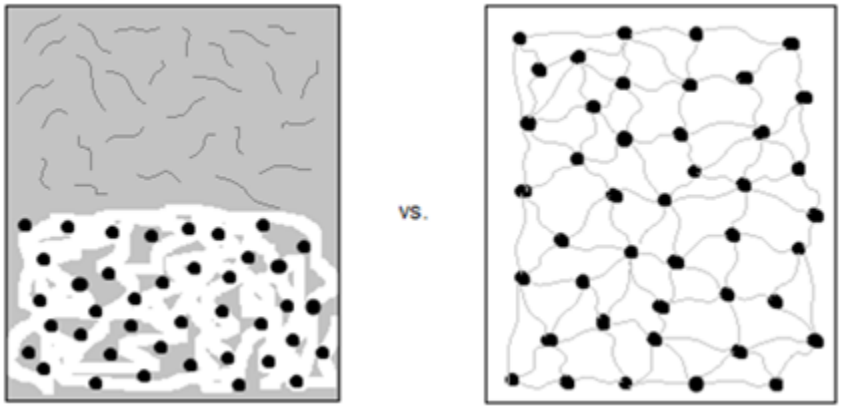

Figure 1.10: Representation of phase separation in conventional epoxy matrix system versus a “matrix-free” composite system.

Due to these newly discovered advantages, the fact that matrix-free approaches allow for maximum loading of nanoparticles (due to lack of domain walls), and the inherent ability to achieve uniform spacing of the nanoparticles in the matrix, exploration of a ‘matrix-free’ composite for use with iron nanoparticles was undertaken as a means to producing more efficient transformer core materials The final goal of my research was to reach a 50% loading, by volume, of nanoparticles to composite.

CHAPTER 2- SOLUTION-BASED PARTICLE SYNTHESIS

2.1 Introduction

Numerous synthetic methods have been published on the formation of magnetic iron nanoparticles.[12, 21, 36] The most illustrative examples of particles that are well dispersed fall into three main synthesis categories: particle size reduction in the solid phase, synthesis via the vapor phase, and synthesis via a liquid phase. Representative methods of the above categories include: high energy mechanical milling,[37] vapor phase deposition,[38] sonochemical decomposition,[39] thin film ceramic decomposition,[40] and thermal decomposition.[27, 33, 41]

For this research, thermal decomposition in the liquid phase was the chosen synthetic route. Thermal decomposition is expected to afford the best control of size, shape and dispersity because the chemistry is relatively simple and requires the use of only one reagent, one surfactant, and a single solvent, with only the evolution of gaseous carbon monoxide (CO) as a byproduct. Advantages of this approach include: the lack of chemical byproducts in the final product make extensive purifications unnecessary, the limited number of starting materials limits the number of concentrations that must be optimized, and the starting materials are all available commercially in high purities.

The thermal decomposition method described in this work to synthesize zero-valent iron nanoparticles used pentacarbonyliron(0), $Fe(CO)_5$ (commonly

referred to as iron pentacarbonyl) as a starting reagent. One might expect the decomposition of $Fe(CO)_5$ would be a straight forward unimolecular decomposition and proceed via first order kinetics. Complications arise, however, from reaction routes involved with the nanoparticle formation reaction. In addition to unimolecular decomposition, a wide range of inter-molecular reactions occur which all depend on the $Fe(CO)_5$ concentration and its many decomposition products. Scheme 1 shows possible reaction mechanisms for the decomposition reaction of $Fe(CO)_5$. Kinetic control of this process is challenging due to this complexity since the order of the reaction changes over time.[41, 42] Nevertheless, control of particle size and dispersity is possible by the careful selection of the solvent and surfactant used in the decomposition reaction.

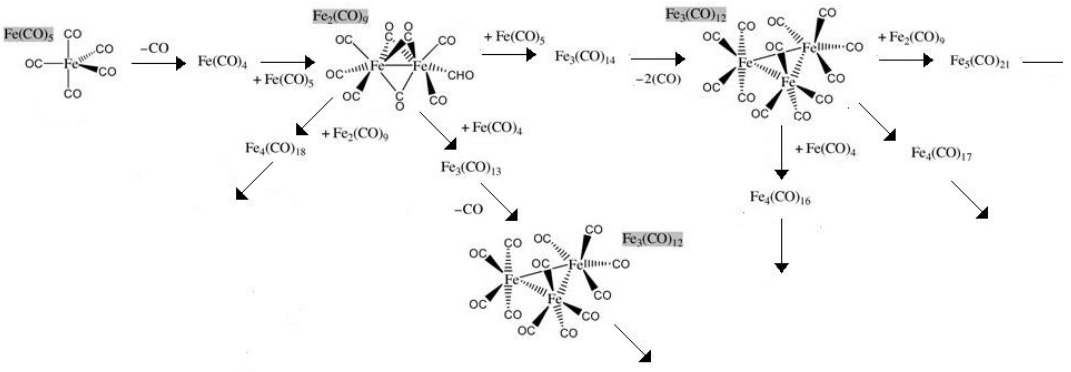

Scheme 1: Decomposition pathways of $Fe(CO)_5$ illustrate the complicated kinetics of the reaction. Only the most likely pathways in the early stages of decomposition, which yield metastable isolable compounds, are shown.

2.2 Reaction Conditions

The reaction conditions used in this research are different from literature methods in several ways and will be discussed in this section. The synthesis of zero-valent iron nanoparticles through an pentacarbonyliron(0) decomposition with an amine surfactant has been published.[33] Here we use a novel method to control the growth kinetics using a slow drip of the iron precursor into the reaction. This drip is designed to allow the nanoparticles to nucleate via magnetic interactions and grow to a critical size where they will precipitate out of solution. Throughout precipitation the drip is continued to promote new nucleation and further precipitation of nanoparticles. This can be repeated as many times as necessary to achieve the desired yield. All precipitated particles are approximately the same size. This approach is patented for the synthesis of zero-valent iron nanoparticles of uniform size and shape.[43] An attempt to scale up the reaction has never been made, although it is theoretically possible. The ability to scale up to large yields is very important for applying this synthesis to the industrial use of producing transformer core materials.

The research was performed with non-purified reagents for the syntheses described here to ensure viability with chemicals of lower grade as may be used in industry. The importance associated to non-purified reagents is to allow for the direct translation into industrial uses where inefficiencies and

high costs associated with purifying expensive chemicals would be unpractical.

The syntheses described herein were performed in an inert atmosphere with reagents that were not treated or purified to remove oxygen or water as has been done in other published syntheses.[28, 44] There are several reasons why the reaction is still expected to produce fully reduced iron, even with unpurified reagents. The reagents spend considerable time well above the boiling point of water while under a flow of nitrogen gas, allowing for the removal of most of the residual water and oxygen in the system. Additionally, the decomposition proceeds with the evolution of 5 moles of CO for every mole of zero-valent iron produced. The atmosphere over the particles is then a mixture of N_2 and CO at very high temperatures, a strongly reducing atmosphere known to reduce oxidized iron to metallic iron, which is used throughout the steel industry.[45]

Another unique aspect of these reactions is the scale. Pentacarbonyliron(0) decomposition reactions are typically on a scale of tens to hundreds of milligrams.[46, 47] In our work we describe reactions on the scale of grams and tens of grams. It is clear from the 1-3 orders of magnitude difference in scale that even the smaller of the two reactions performed for this work is enormous in comparison to typical literature reactions. The ability to increase scale to such a degree, confirms the relevance to industrial applications, as even further scaled up reaction yields may be necessary in the future.

The main issues that arise with scaling up reactions are difficulty controlling heat and mass transport.[48] In small molecule chemistry these problems may lower yield, but in nanoparticle synthesis they can cause difficulty in size and shape control.

2.3 Experimental

2.3.1 Methods and Materials

All chemical transformations were carried out with the rigorous exclusion of air and water using standard Schlenk-line and glovebox techniques. All chemicals and reagents were purchased from Sigma-Aldrich (St. Louis, MO): dioctyl ether (DOE, an anhydrous solvent), dodecylamine (99% purity), and anhydrous pentacarbonyliron(0), $Fe(CO)_5$, were used as received.

2.3.2 Synthesis Details

2.3.2.1 Synthesis of zero-valent iron nanoparticles via decomposition of pentacarbonyliron(0) in the presence of an amine surfactant

A 100 mL 3-neck round bottom (r.b.) flask was used, attached to a water cooled reflux condenser under flowing N_2. Septa were inserted into two of the three necks and needles were used to provide a nitrogen input and the controlled addition of reagent. The N_2 was flowed through the reaction and out through a needle attached to a hose adapter fitted to a bubbler. A cross-bar magnetic stirrer was added to the flask. The reaction set-up was purged with N_2 for 30 minutes.

The reaction flask was charged with 20 mL of dioctyl ether (DOE) and 400 mg of dodecylamine. The reaction flask was placed in a stabilized oil bath at 220 ºC while being purged under N_2 for another 30 minutes. The solution was set to stir at 250 rpm, to maintain vigorous mixing. 3 mL of $Fe(CO)_5$ and 17 mL DOE was injected into the flask through a five inch long stainless steel needle at a rate of 4 mL per hour for a total of 5 hours using an automated programmable syringe pump.

The orange colored pentacarbonyliron(0) turns black upon nucleation of iron nanoparticles. Nucleation times were measured after addition of $Fe(CO)_5$ and subsequent formation of a black precipitant. The color change occurred after the first few drops of Fe(CO) were introduced, which suggests that nucleation occurs rapidly. Rapid reaction rates can cause problems with size control and dispersion. These two factors were analyzed using small angle X-ray scattering (SAXS) and thermogravimetic analysis (TGA).

After the entire contents of the syringe were injected into the flask, the reaction was allowed to continue for 30 additional minutes to permit any remaining $Fe(CO)_5$ to finish reacting. The extra time produced better yields and prevent contamination by unreacted $Fe(CO)_5$. After completion, the reaction flask was capped under N_2 flow, all three rubber septa were wired into place, and the reaction flask was brought into a nitrogen glovebox. The particles were transferred into a secondary storage container while in the glovebox. It is worth mentioning the difficulty with which the particles were

removed from the stir bar. The majority of the particles synthesized were agglomerated and magnetically attached to the stir bar. It was only after much time and manipulation with two powerful magnets, that the particles were transferred off of the stir bar into the secondary storage container for characterization and further reaction. The magnetic characteristic of these synthesized particles was first shown in Figure 2.1 by manipulation of the particles in a magnetic field.

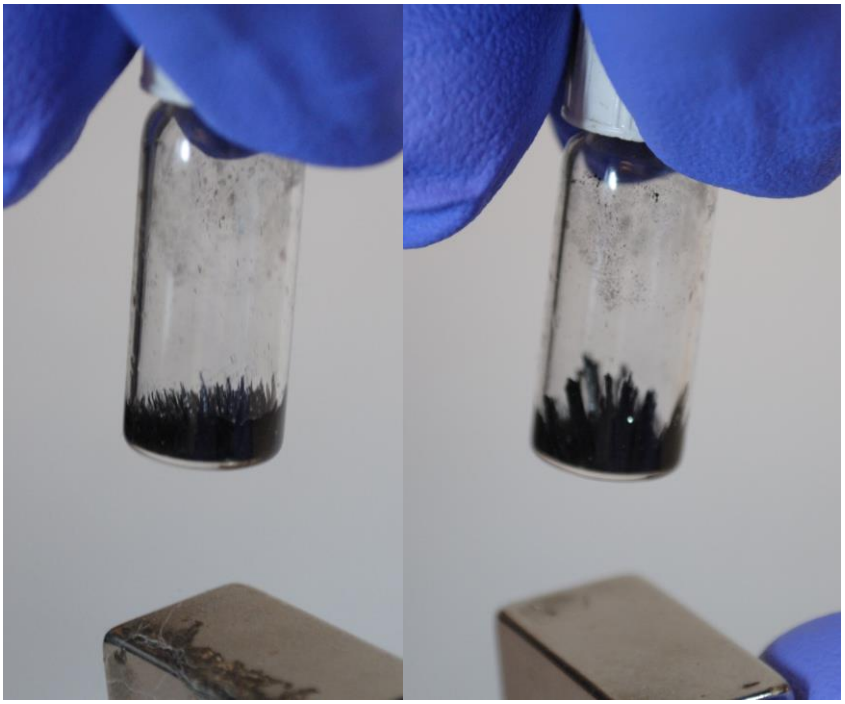

Figure 2.1: Effect of a strong permanent magnet on zero-valent iron nanoparticles (~13 nm).

These particles were characterized by DC Magnetometry, TGA, SAXS, and transmission electron microscopy (TEM). A brief description and the data and

results of all of these analyses are included in the results section of this chapter.

2.3.2.2 25-fold scale up of iron nanoparticle synthesis

For the scaled up reaction, many of the same setup requirements were the same as in the first synthesis. The use of larger equipment, such as a 1 L 3-neck r.b. flask and a 3 inch egg-shaped magnetic stirrer were needed to handle the increased volumes of the reaction.

The reaction flask was charged with 300 mL of dioctyl ether and 4.819 g of dodecylamine. This reaction was also heated to 220 ºC, but the solution was set to stir at only 200 rpm, due to the larger volume of the reaction and increased distance between the glassware, heating mantle, and stir plate.

The syringe solution was prepared by adding 45 mL of $Fe(CO)_5$ to 255 mL of DOE. The final volume to be added to the reaction flask was 300 mL, for a total reaction volume of 600 mL. A 60 mL plastic syringe was used for the injection of the solute. A long 18 gauge needle was bent to a sloping 80 degree angle and inserted into the flask through the septa. Due to the large volume of solute to be added to the flask solution, multiple 60 mL aliquots were used to inject the solute into the flask. The rate of injection was 60 mL per hour using an automated programmable syringe pump which therefore required 5 syringe changes, one each hour.

Approximately 2 min. after the syringe pump was started; nucleation of the reaction appeared to have occurred because of the darkening of the solution to a dark brown or black. After the last aliquot of solute was added to the reaction flask, the reaction was heated for 30 additional minutes to ensure that all of the $Fe(CO)_5$ had finished reacting. The reaction flask was then removed from the heating mantle and allowed to cool to room temperature. While still warm, the water reflux condenser was removed from the flask and a gas adapter with a Teflon stopcock was put in its place. The second neck was sealed with a glass stopper and the septum on the third neck was zip tied in place. Each time the reaction vessel was opened, a strong flow of nitrogen was provided to maintain the inert atmosphere. The flask was put under vacuum for 10 minutes to remove the dissolved CO before being brought into the N_2 glove box. The sealed flask was brought into the nitrogen glove box to be transferred into a secondary storage container. The magnetism of the particles was again verified through the use of a strong permanent magnet (Figure 2.2).

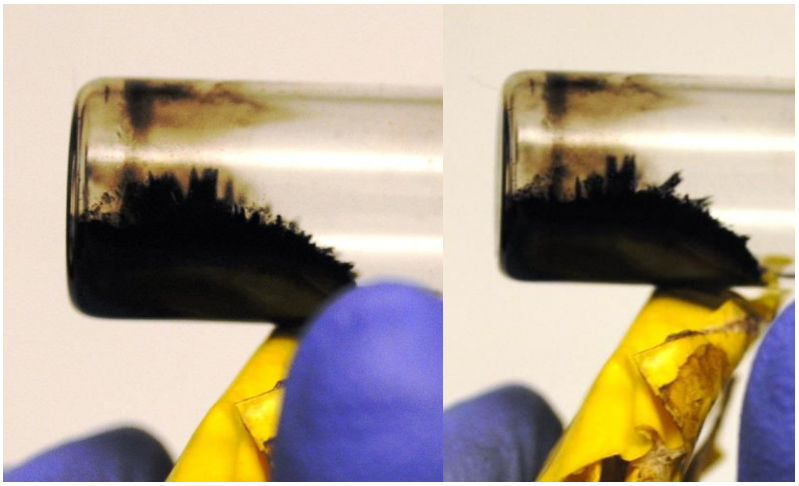

Figure 2.2: Magnetic effect on zero-valent iron nanoparticles synthesized in a large scale reaction.

The magnetically precipitated particles were separated from the supernatant since it contained smaller particle nucleations which didn't have sufficient reactant and/or time to grow into full sized particles and precipitate out of solution. These larger precipitated nanoparticles were rinsed three times with purified and degassed hexane to remove excess surfactant and DOE from the nanoparticle surfaces. The particles were characterized by DC Magnetometry, SAXS, and TEM.

2.4 Results and Discussion

2.4.1 Thermogravimetric Analysis (TGA)

A NETZSCH Jupiter STA 449F1 Thermogravimetric Analyzer (TGA) with a CC300 automated Liquid Nitrogen Dewar system and NETZSCH Measurement Software (version 6.0.0) was used to analyze the iron

nanoparticles synthesized. This instrument has the capability to run both TGA and DSC analyses simultaneously. This is a single analysis, manual loading instrument with programmable temperature ramping and programmable cover gas flow rates. For uniformity, all samples were run with the same program, starting at 40 ºC and ramping up to 600 ºC at a rate of 10 ºC per minute for 60 min. This temperature was then held for 45 min. for a total run time of 120 min. The hold at 600 ºC was to ensure that a stable final weight was reached and recorded. NETZSCH Proteus Thermal Analysis Software (version 6.0.0) was used to analyze and quantify the TGA results.

Sample weigh boats were tared on the instruments' internal balance and loaded with the sample, consisting of iron nanoparticles in a minimum volume of hexane. The initial weight was recorded by the operator and the instrument, and the program was started. All graphed data is presented in percent loss and the values in the table are converted to total mass loss (in mg) of the sample. In Figure 2.3, the initial mass loss shown, from 100% to approximately 66% is the loss of the hexane solvent (hexane, b.p. 69 ºC)[11] that the nanoparticles were stored in.

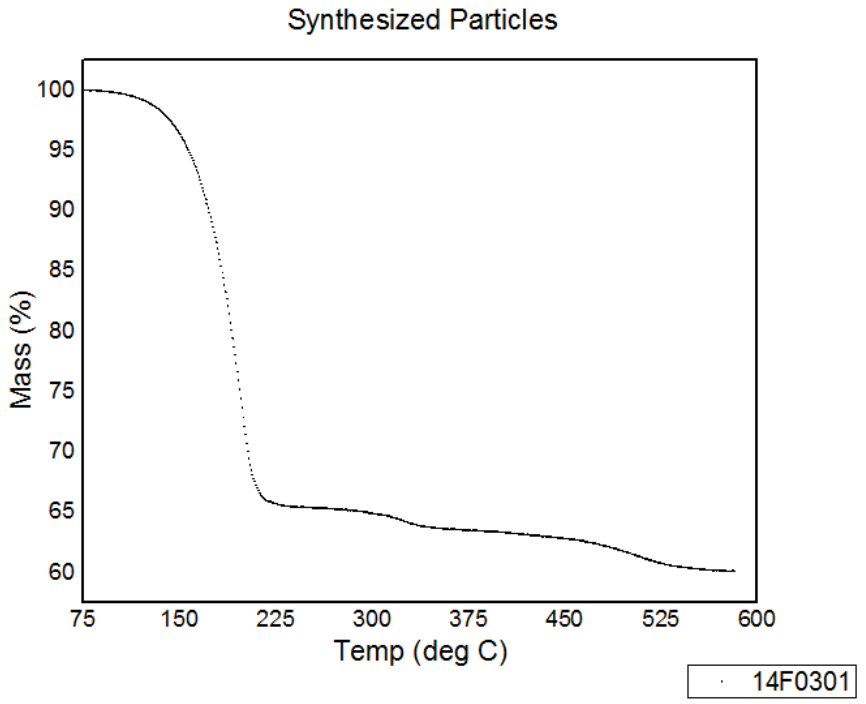

Figure 2.3: Raw TGA Data of Synthesized Zero-Valent Iron Nanoparticles.

Table 2.1: Nanoparticle Synthesis Mass Loss by TGA

Sample	Initial Weight	Final Weight	Mass Loss	Percent Loss
Small Scale	23.870 mg	21.841 mg	2.029 mg	8.502 %

The remaining loss of mass in the sample is due to the surfactant, dodecylamine (b.p. 248 ºC)[11] attached to the surface of the nanoparticles and any trace remnants of DOE (b.p. 286 ºC)[11] in the TGA sample. No other chemicals are involved in the synthesis of the nanoparticles and therefore all loss is attributed to the chemicals mentioned above. There was an 8.5% loss for the small scale synthesis reaction.

The more surfactant there is in the sample, the more dilute the magnetic properties of the sample will be. For this research, maximizing loading of the particles into the final composite is one of our goals. The small mass loss seen by TGA is good, since it implies that little surfactant is present in the sample. The TGA of the small scale synthesized particles acts primarily a baseline measurement for future comparison of modified particles. Although the mass loss of surfactant can be used to estimate the particle size, we performed detailed size analysis using SAXS and TEM.

2.4.2 DC Magnetometry via Superconducting Quantum Interference Device (SQUID) Magnetometry

An MPMS SQUID magnetometer (made by Quantum Design) was used for sample measurements. A SQUID is a sensitive magnetometer used to measure extremely subtle magnetic fields. A typical SQUID magnetometer can detect a magnetic moment as low as 10^{-10} A•m^2. The MPMS system includes: a temperature control system which allows for a temperature range of 2 to 400 K, a superconducting magnet capable of generating fields up to 7 T; a SQUID detector and amplifier system, a sample handling system to control the motion of the sample through the pick-up coils, and a computer operating system.

In this magnetometer, the SQUID is not used to directly measure the sample's magnetic field. Instead, it is located almost 11 cm below the

instrument's superconducting magnet, inside of a superconducting shield. The SQUID is connected to superconducting pick-up coils which sit outside of the sample space via superconducting wires. The sample is transported through superconducting detection coils connected to the SQUID. The magnetic moment of the sample induces an electric current in the coils which is converted to an output voltage in the SQUID and is proportional to the sample's magnetic moment. In essence, the SQUID magnetometer actually functions as an extremely sensitive linear current-to-voltage detector.

There are two standard magnetometry measurements that are commonly performed on magnetic nanoparticles. The first measurement is commonly referred to as a temperature sweep. This is performed by cooling the sample to cryogenic temperatures (10 K) in the absence of a magnetic field, applying a weak magnetic field (commonly 1 mT) before warming to room temperature, and finally cooling to 10 K a second time with the same applied field.

The second standard measurement produces standard hysteresis plots, and can be referred to simply as a field sweep, especially in cases where samples do not demonstrate significant magnetic hysteresis (as is the case with some of the samples analyzed in this research). To do this, the temperature is held constant while the applied magnetic field is ramped from zero to a strong, saturating field. The field is swept from the saturating field to an equal field in the opposite direction, returning again to the initial saturating field. Both of

these measurements are used to characterize the magnetic properties of samples analyzed by the DC SQUID magnetometer.

The preparation of the samples for SQUID measurements is important. Analyzing liquid samples, such as nanoparticles dispersed in a solvent, would allow for large scale motion of the particles in the externally applied field. This motion can introduce significant particle-particle interactions that make data interpretation difficult. To analyze nanoparticles using this method, therefore, the particles must be evenly dispersed into a solid, non-conductive matrix, such as docosane ($C_{22}H_{46}$, m.p. 44.4 °C).[11] Samples that were vigorously mixed in molten docosane were loaded into 5 mm (OD) NMR tubes and were uniformly solidified by quick cooling. Since the instrument can run higher than the melting point of docosane, the temperature was capped at 300 K to prevent re-melting and reintroducing particle motion.

The sample introduction and transport system for the SQUID magnetometer is shown in Figure 2.4. It is important to center the sample within the sample transport system before analyzing by DC, as failing to do so results in a misbalance in the sample transport system and possible instrument damage. The sample chamber is kept under vacuum throughout the measurement.

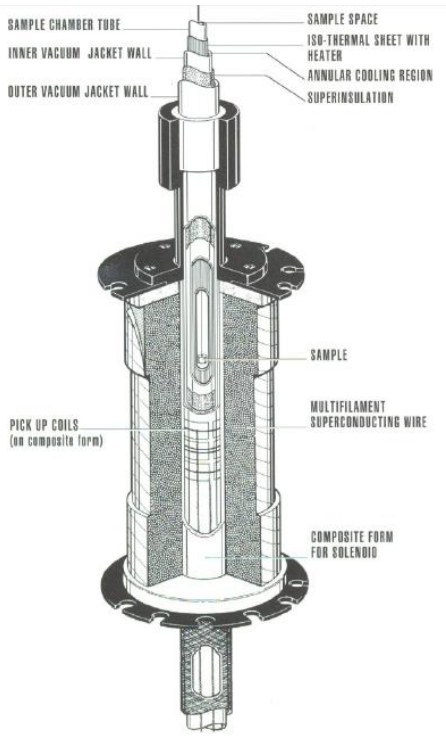

Figure 2.4: Schematic drawing of the major components surrounding the sample in the SQUID MPMS. Image courtesy of Quantum Design, Inc.

The data gathered from the standard measurements on the initial iron nanoparticle synthesis are shown in Figure 2.5. For the temperature sweep (Figure 2.5(a)), the sample was cooled to 10 K in the absence of a magnetic field, a weak, 1 mT, magnetic field was applied and the sample moment was measured. The temperature was increased in this field and moments were measured at 5 K intervals up to 300 K. This set of measurements constitutes the Zero-Field Cooled (ZFC) curve denoted by red triangles in Figure 2.5 (a). This nomenclature is standard and explains that the sample was cooled in the absence of an applied field.

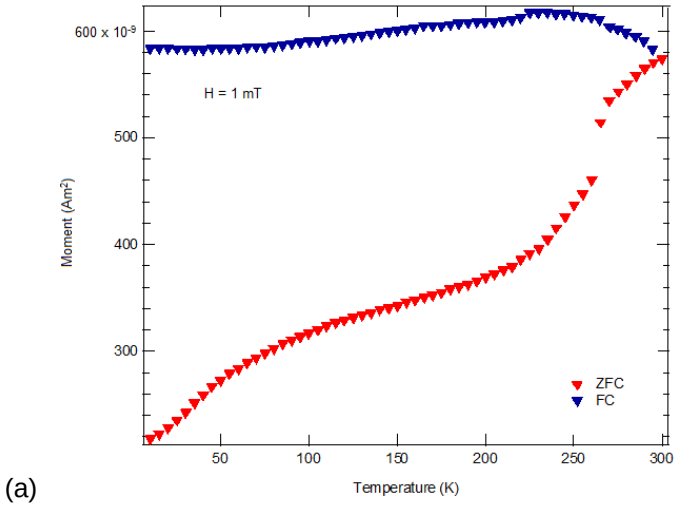

(a)

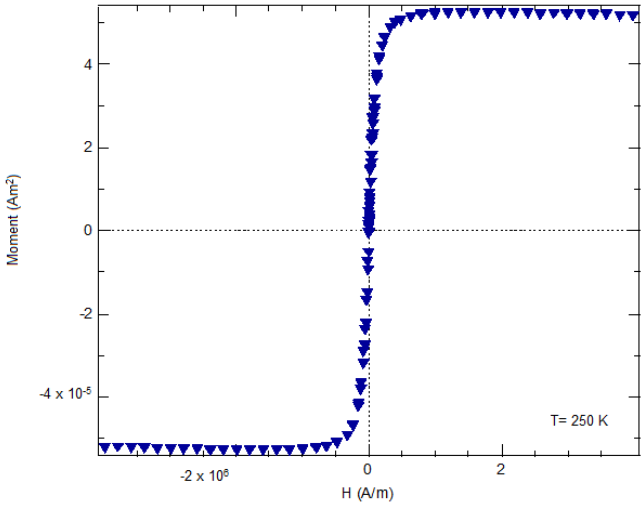

(b)

Figure 2.5: SQUID Data for Synthesized Zero-Valent Iron Nanoparticles. (a) ZFC / FC magnetization curves for nanoparticles with an applied field of 1 mT. (b) Magnetization curve of particles at 250K.

In the ZFC curve, the applied field remains constant, but the thermal energy provided to the iron nanoparticles does not. Since the magnetization of a single domain magnetic nanoparticle is a thermally activated process (as described in Chapter 1), the additional thermal energy gained through heating

allows the spins of the nanoparticles to better align with the external magnetic field. This is why ZFC curves of single domain particles (below their blocking temperature, T_B) show only increasing moment with increasing temperature.

The fact that these particles do not show a decrease in moment at any temperature during the warming cycle indicates that the temperature does not exceed the T_B of the sample. The data does, however, contain one unexpected feature: a noticeable jump in moment between the 260 and 265 K measurements. This unexpected feature is likely due to the melting of a residual quantity of DOE (m.p. 265 K)[11] in the sample that remained from the original synthesis. The melting of this residual solvent would be expected to possibly allow some of the particles to physically move to orient better with the applied field. This anomaly is small and does not significantly detract from the analysis. As such, we can ignore the anomalous increase and see that the rate of increase of the moment is slowing towards the end of the ZFC curve. This implies that the sample is nearing the blocking temperature of the particles.

At 300 K, the heating is stopped and the sample is cooled under the same constant externally applied field. The measurements taken during this cool down cycle make up the Field-Cooled (FC) curve that is denoted by blue triangles in Figure 2.5 (a). In ideal Néel-Brown behavior, the FC curve below T_B is flat and featureless. This is because particle spins do not reorient as thermal energy is removed from them and they freeze in place. In reality,

small variations in the FC curve below T_B are observed and are often attributed to non-Néel-Brown behavior. This behavior can involve “surface spins” which are the magnetic spins of some portion of atoms at the surface of a particle that are, at least partially, misaligned with the overall particle moment. These spins represent a small departure from Néel-Brown behavior and are the reason for the departure from a completely flat FC curve in Figure 2.5(a). The difference is not important for the proposed application of these nanoparticles, and the physics of this phenomenon are beyond the scope of this thesis.

The significant difference between the ZFC and FC curves at all temperatures analyzed indicates that the particles are still blocked (below the T_B) in the entire temperature range of the analysis. If the particles were above their blocking temperature they would be labeled unblocked and be superparamagnetic, therefore showing ZFC and FC curves overlaid in the graph since superparamagnetic particles have no magnetic hysteresis.

Figure 2.5 (b) shows the data from a field sweep at 250 K. We know from the temperature sweep that the particles are below their blocking temperature at 250 K and therefore exhibit hysteresis, but the field sweep shows a hysteresis loop that is far from typical bulk iron. Though iron is considered a soft magnet, it’s remnant magnetization (the magnetization that remains upon removal of an applied magnetic field) is typically near 80% of its saturation value.[49] The remnant magnetization measured for the iron nanoparticle is more than an

order of magnitude lower, being approximately 5% at 250 K. At 300 K we would expect it to be lower still, completely disappearing at and above the T_B of the sample.

The difference in the shape of the magnetization curve, as compared to a bulk material (as shown in Figure 1.2), is worth mentioning. For single domain particles, the susceptibility (slope of the curve of magnetization versus applied field) begins very high and then decreases. For multi-domain particles, the susceptibility begins at an intermediate value, increases to a maximum near 50% of saturation, then decreases.

The magnetic behavior observed is what is expected for particles with a T_B just above room temperature. It also provides a baseline for future measurements, where the goal will be to maintain these magnetic properties while scaling up the size of the reaction, modifying the particle surfaces, and forming a nanocomposite.

Companion data from the magnetic characterization of the scaled up reaction are presented in Figure 2.6. The data is similar, indicating that the particles synthesized are of similar shape and size. Notable differences in the data will be individually discussed.

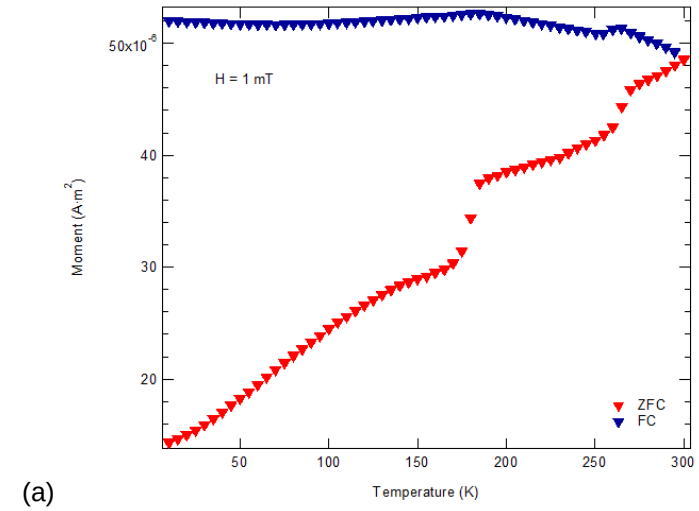

(a)

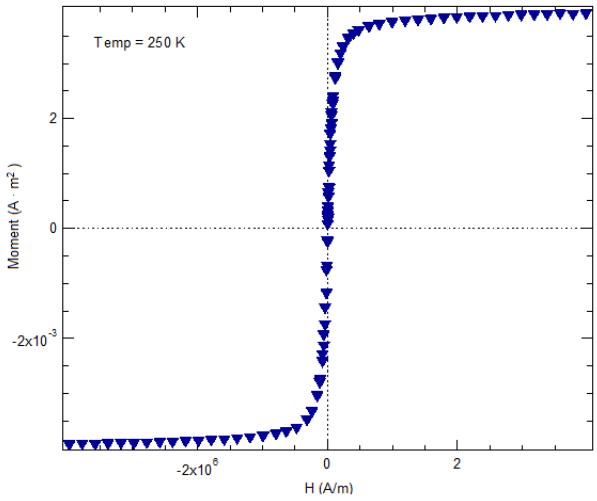

(b)

Figure 2.6: SQUID data for 25-fold scale-up synthesized zero-valent iron nanoparticles. (a) ZFC / FC magnetization curves for nanoparticles with an applied field of 1 mT. (b) Magnetization curve of particles at 250K.

The temperature sweep, most noticeably the ZFC, is different due to the presence of two anomalous increases in magnetic moment, where the previous data had only one. These increases occur between 175 and 180 K and between 260 and 265 K. The increase above 260 K has already been

attributed to the melting of DOE. This sample was washed with hexane in an attempt to remove excess DOE which explains why the increase due to DOE is of lower magnitude than the one visible in Figure 2.5. The additional increase above 175 K is attributed to the melting point of hexane (178 K).[11] Again, the decrease in slope of the ZFC curve near the maximum temperature indicates that the sample is approaching its T_B. The field sweep for this sample is nearly indistinguishable from the previous sample. The absolute values differ due to the differing quantities of iron in the two samples. This is one confirmation that the two separate reactions produced particles with the same magnetic characteristics.

Overall, the scaled-up reaction behaves nearly identically to the sample from the smaller-scale reaction. This shows that in the property that matters most, for the application in transformer cores, the scale-up was successful.

2.4.3 Small Angle X-Ray Scattering (SAXS)

The scattering of X-rays by electrons in a material can be used to measure the average spacing between planes of atoms, determine crystal orientation, identify crystal structure, and measure crystallite size and shape. [50] High angle X-ray diffraction gives information about a crystal structure at the atomic scale and can be used to estimate crystallite size. [50]

Small angle X-ray scattering (SAXS) however, observes only lower angles and is not sensitive to the structure of the crystal. Instead, it provides

structural information on a larger scale and therefore gives information as to the size of a nanoparticle.[51] SAXS was used in this work to determine the average size of an ensemble of nanoparticles.

In order to disperse the particles into a uniform distribution for analysis, some sample preparation was necessary. An aliquot of iron nanoparticles in hexane was added to an equal volume of oleic acid at 65 ºC for 60 min. in air. This removed the hexane solvent and oxidized the zero-valent iron nanoparticles to Fe_3O_4, magnetite, by taking advantage of oleic acid's known propensity to oxidize iron nanoparticles.[33] This chemical change explains why the particles dispersed into the solution so well: they were less magnetic. This sample preparation has two effects that change the final size of the particles analyzed. The decrease in density from iron to magnetite and the increase in volume from the addition of oxygen to the iron together give an expected 2.1 fold increase in the volume of the particles. This volume increase translates to a 1.28 fold increase in the diameter of the particles when converted from zero-valent iron to magnetite. The actual diameter of the synthesized particles should therefore be only 78% of the measured diameter in SAXS. The measurements of the size of the magnetite particles must then be reduced appropriately to reflect the pure iron.

The prepared particles were then injected into 1.0 mm glass capillary tubes. All samples were analyzed using a Rigaku SmartLab diffractometer System in SAXS mode with SmartLab Guidance system control software (Figure 2.7).

CuKα radiation (40 kV, 44 mA) was used in transmission geometry with a scintillation detector.

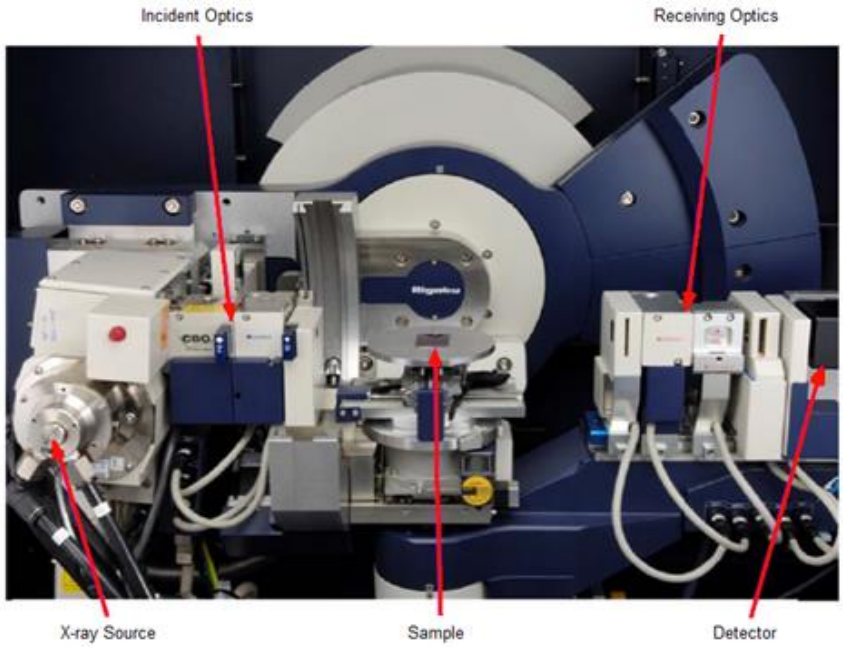

Figure 2.7: Rigaku SmartLab X-ray diffractometer with parallel beam optics. Image courtesy of Rigaku Americas Corporation.

The scattering of X-rays occurs when the electron density of the nanoparticles differs from the electron density of the matrix in which the particles are suspended when irradiated.[51] The size distribution can be extracted from this scattering profile through the use of a normal distribution model which is assumed for, and fit to, the nanoparticle data. Least squares fits were performed on the data using Rigaku NANO- solver v.3.5 software. A spherical model was applied and a volume average diameter was calculated. The SAXS technique is well known for its ability to provide particle size distributions for an ensemble of particles as they are being measured. This

differs from other methods in that it allows for a more comprehensive statistical result than electron microscopy for example.

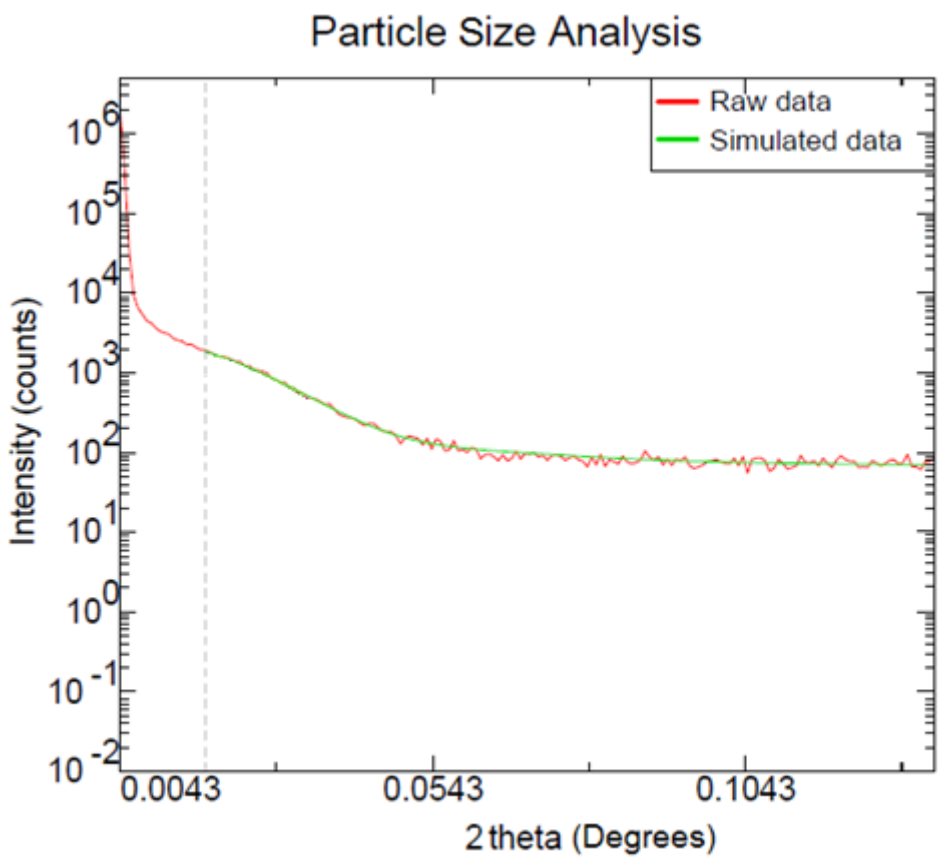

Figure 2.8: SAXS results for the small scale synthesis of iron nanoparticles. Raw SAXS data (red) and simulated data (green) that represent the particle size distribution fit with a normal distribution and an average size of 15.9 nm with a 20% dispersion for iron nanoparticles oxidized to magnetite. The fit does not extend to very low angles due to the appearance of the edge of the direct beam. The vertical dotted line represents the lower limit of the fit.

The SAXS data and fit for the initial, small scale reaction (Figure 2.8) yields a mean particle size of 15.9 nm with 20% dispersion for particles that have

been oxidized to magnetite. Accounting for the particle expansion upon oxidation, yields a calculated size of zero-valent iron nanoparticles of an average 12.4 nm in size with 20% dispersion. The fit calculations assume spherical particles with a normal distribution of particle sizes.

The large scale reaction SAXS data and fit for the oxidized, un-agglomerated iron nanoparticles (Figure 2.9) were 11.9 nm with 26.5% dispersion. The oxidized, magnetically agglomerated, and precipitated iron nanoparticles (Figure 2.10) were 12.5 nm with 28.5% dispersion. These particle sizes reduce to 9.3 nm and 10.0 nm for the zero-valent iron nanoparticles, respectively. All of the SAXS data recorded from both the initial iron nanoparticle synthesis and the 25 times scale up reaction showed nanoparticles less than 15 nm in size with dispersion less than 30%. This confirmed that the synthesis method produces uniform magnetic nanoparticles.

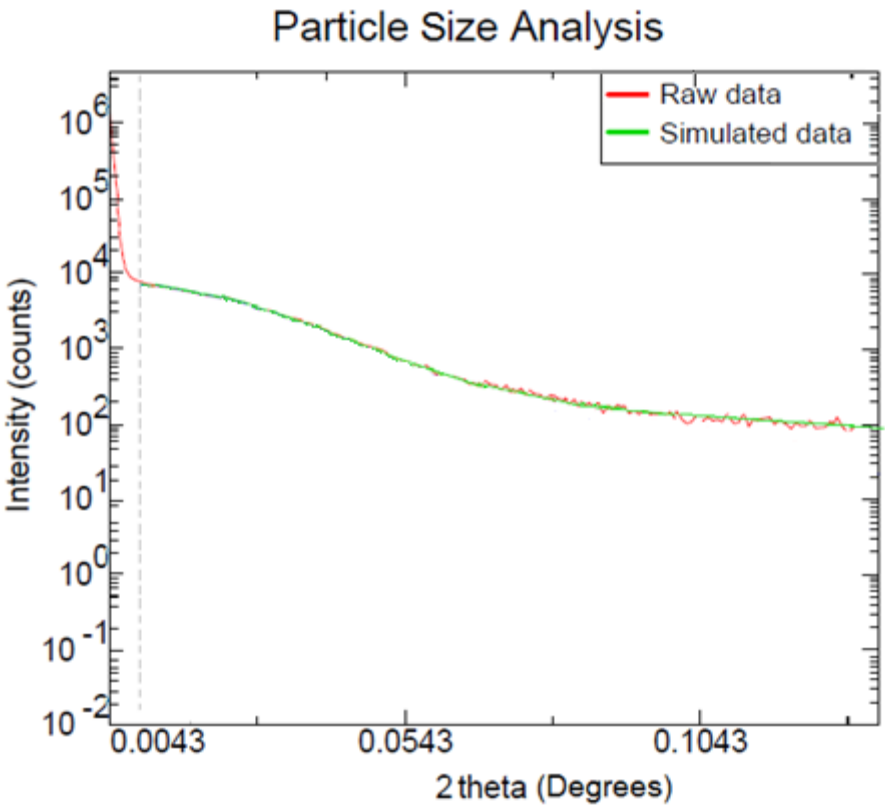

Figure 2.9: SAXS results for the supernatant in the scaled-up synthesis of iron nanoparticles. Raw SAXS data (red), simulated data (green) that represent the particle size distribution fit with a normal distribution and an average size of 11.9 nm with 26.5% dispersion for iron nanoparticles oxidized to magnetite. The fit does not extend to very low angles due to the appearance of the edge of the direct beam. The vertical dotted line represents the lower limit of the fit.

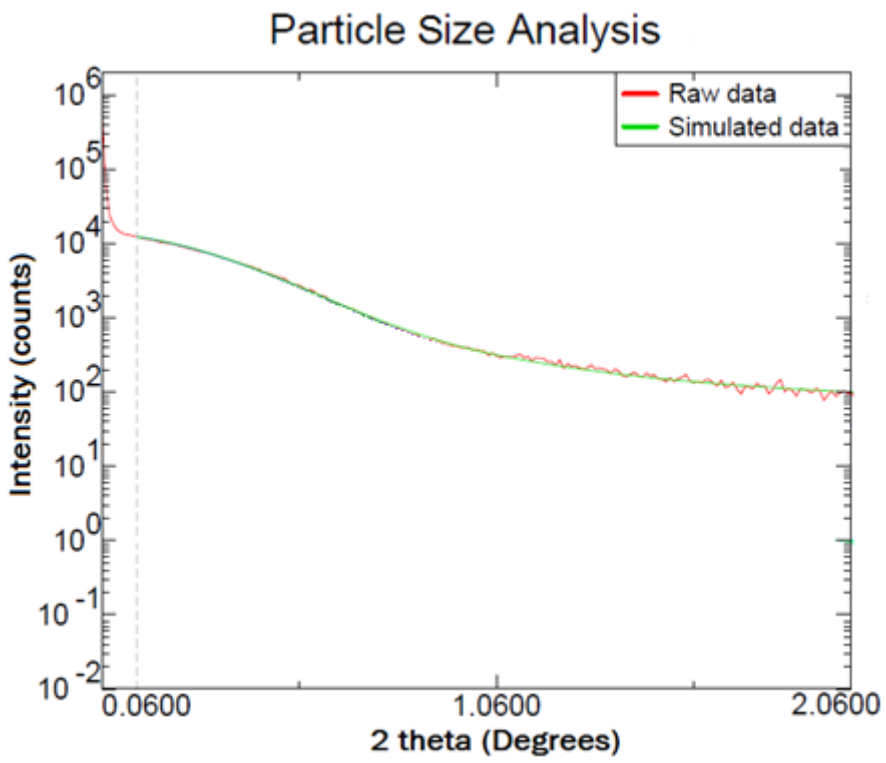

Figure 2.10: SAXS results for the precipitated particles in the scaled-up synthesis of iron nanoparticles. Raw SAXS data (red), simulated data (green) that represent the particle size distribution fit with a normal distribution and an average size of 12.5 nm with 28.5% dispersion for iron nanoparticles oxidized to magnetite. The fit does not extend to very low angles due to the appearance of the edge of the direct beam. The vertical dotted line represents the lower limit of the fit.

2.4.4 Transmission Electron Microscopy (TEM)

Transmission electron microscopy uses high energy electrons focused into a very thin beam transmitted through a thin (i.e. electron transparent) sample to image and analyze the structure of materials, with atomic resolution for high resolution TEM.

The electron beam is focused with electromagnetic lenses, and depending on the density of the material present, some of the electrons are scattered and disappear from the beam, while the remaining (i.e. transmitted) electrons are focused and magnified for observance on a phosphorescent or fluorescent screen at the bottom of the microscope column and recorded digitally. The image of the sample is displayed in varying shades of gray and black according to the density of the different parts of the sample. The electrons that are focused in the beam are accelerated up to several hundred keV, which generates wavelengths that are much smaller than those of visible light, allowing for the high resolution of the images taken by a TEM over that of a conventional microscope.

The TEM employed in this work was a JEOL 1200 EX with a tungsten hairpin filament and approximately 0.5 nm spatial resolution (JEOL USA, Inc., Peabody, MA). Images for size analysis were acquired in bright field mode at an acceleration voltage of 120 keV and processed using ImageJ software. A statistical number of particles were measured individually for size and the averages were calculated for the particles over the entire range of TEM images taken for the sample.

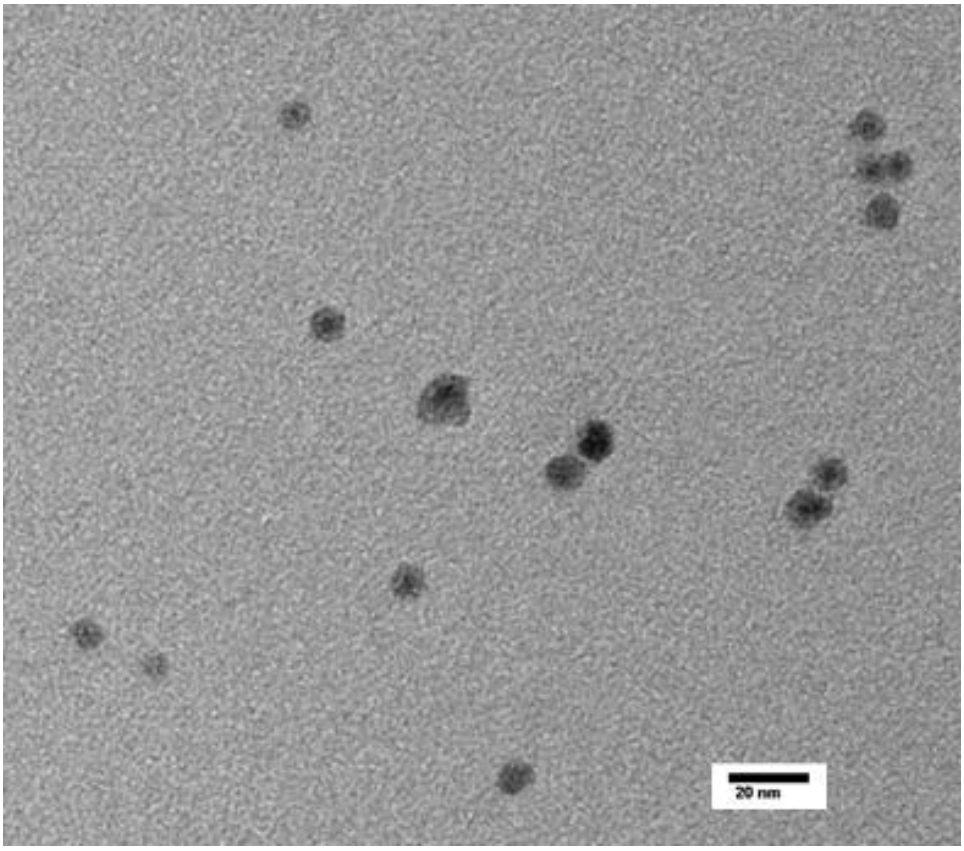

Figure 2.11: TEM image of iron nanoparticles in the surfactant of the small scale synthesis via $Fe(CO)_5$ and dodecylamine.

The non-agglomerated nanoparticles in the supernatant of the small scale reaction (Figure 2.11) were measured to be between 3 and 15 nm, with an average size of approximately 9 nm. This brings us to the conclusion that these particles initally nucleated, but did not have enough time to increase in size as the magnetically separated nanoparticles did. A separate SAXS measurment of the supernatant particle size was not performed, so there is no comparison available for the TEM measurement. The three other TEM measurements can be directly compared to their SAXS measurements.

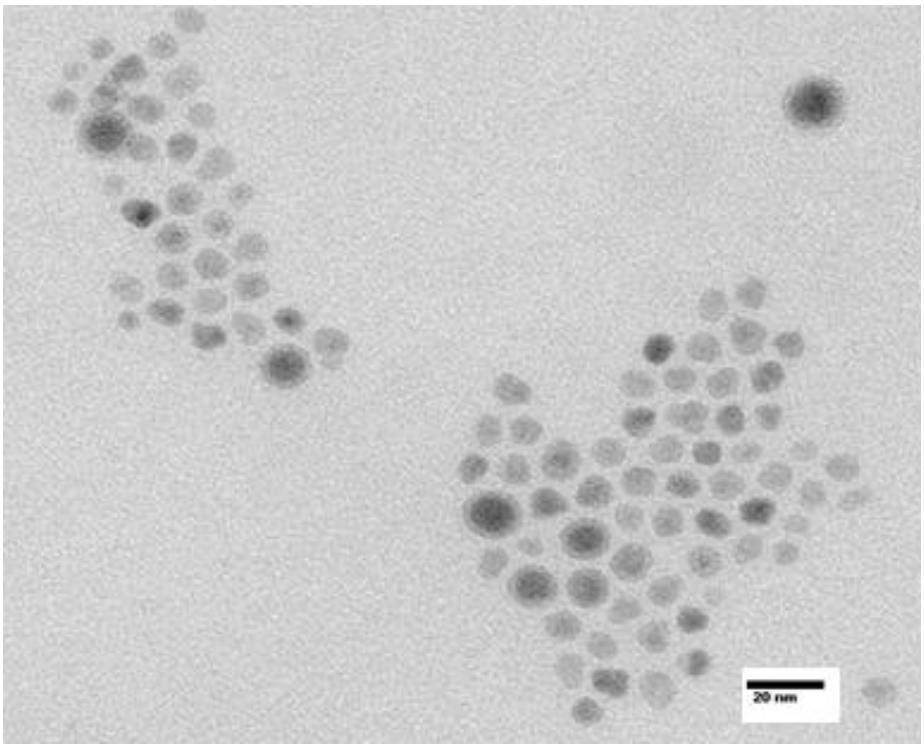

Figure 2.12: TEM image of iron nanoparticles in the magnetically agglomerated portion of the small scale synthesis via $Fe(CO)_5$ and dodecylamine.

The TEM images taken of the agglomerated nanoparticles (Figure 2.12) showed a size range of 7 to 22 nm, with an average size of approximately 13 nm, which generally agrees with the SAXS data. The size distributions of the particles in Figure 2.13, are shown as histograms and agree with the SAXS data.

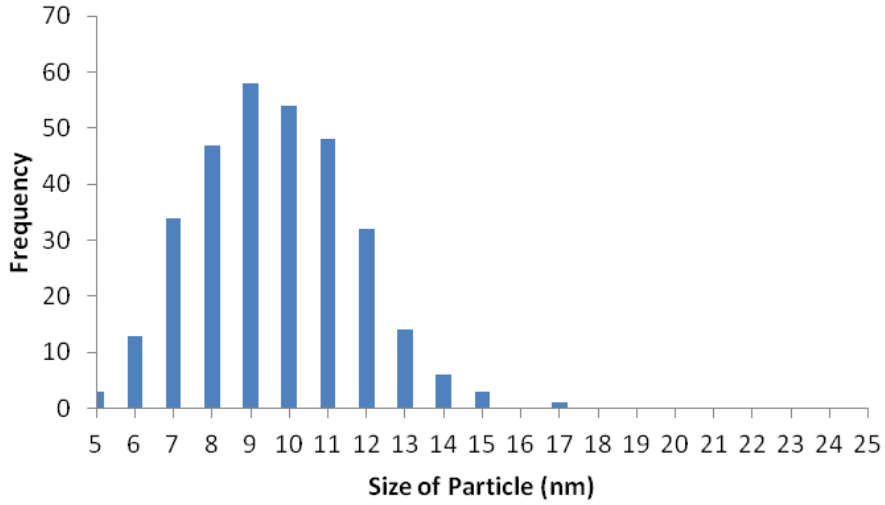

(a) Histogram of size distribution from the initial nanoparticle synthesis supernatant.

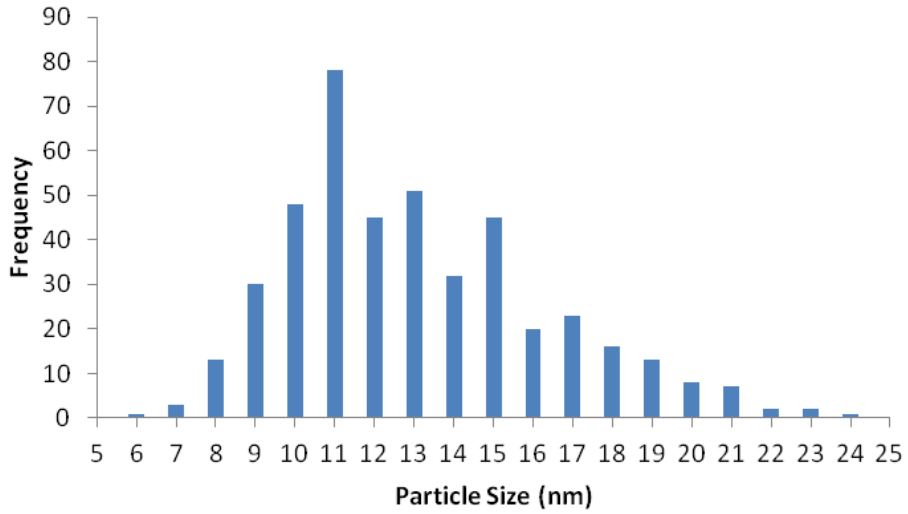

(b) Histogram of size distribution from the initial nanoparticle synthesis magnetic agglomeration.

Figure 2.13: Histograms of synthesized particles measured in TEM images of (a) the supernatant and (b) magnetic agglomerates.

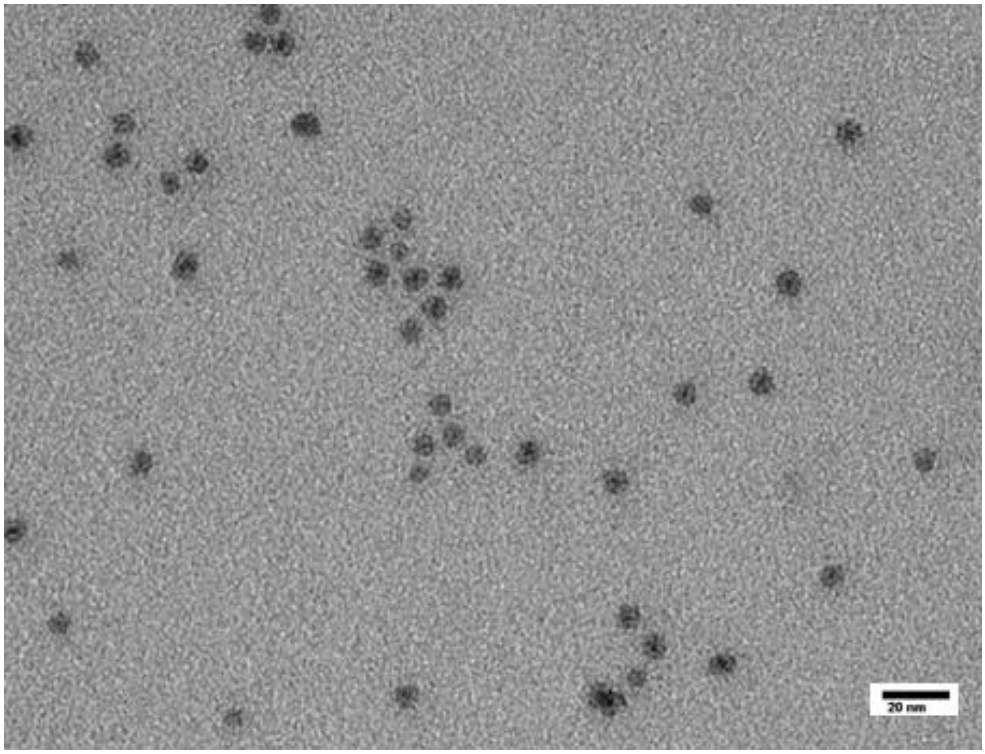

Figure 2.14: TEM image of large scale iron nanoparticle synthesis supernatant by way of $Fe(CO)_5$ decomposition and dodecylamine surfactant.

The nanoparticles sizes in the supernatant from the large-scale reaction (Figure 2.14), were calculated to be between 7 and 11.5 nm, with an average size of approximately 9 nm. This generally agrees with the previous synthesis which shows that the synthetic method produces consistent sized nanoparticles that depend on the reaction conditions.

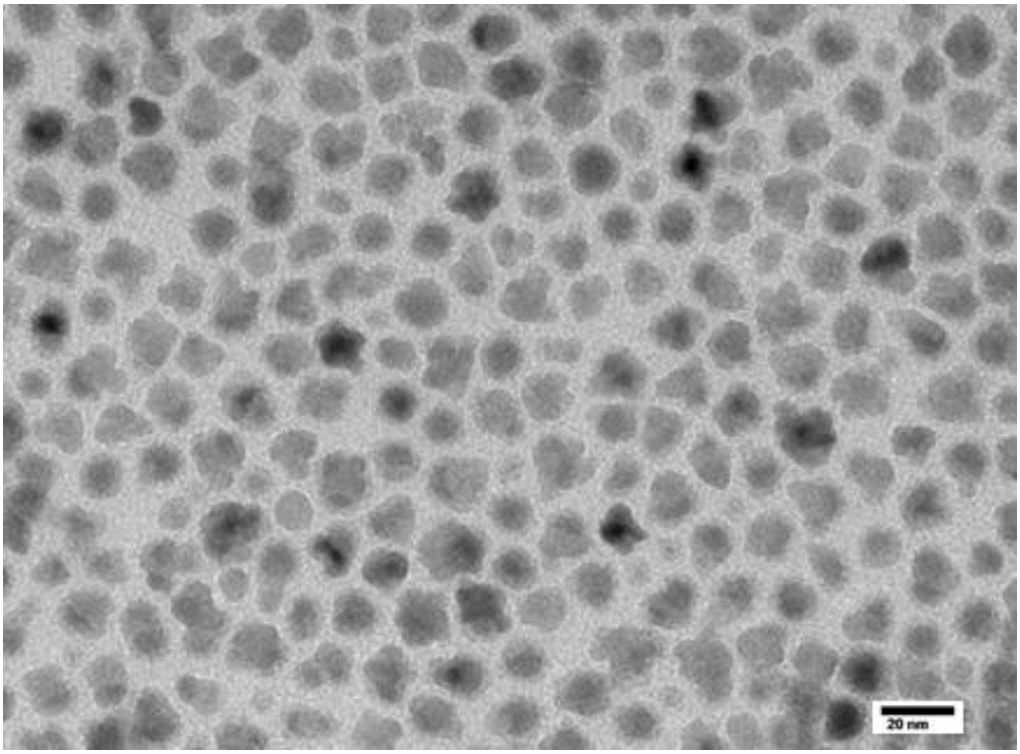

Figure 2.15: TEM image of a magnetic iron nanoparticles made by a large scale synthesis using $Fe(CO)_5$ and dodecylamine.

The nanoparticles that were magnetically separated in the scaled-up reaction (Figure 2.15), were measured to be between 8 and 22 nm, with an average size of approximately 13 nm. These nanoparticles are highly magnetic and have a zero valent iron core that is surrounded by a thin layer of iron oxide. The oxide layer likely formed during TEM sample preparation, as this was performed in air. Some of the TEM images showed non-spherical shapes for these particles and also some very large agglomerations. These images show that the fine tuning of size and shape in synthesis reactions on this large of a scale are very difficult to control. The extremely rapid reactions observed in

the large scale reaction likely led to the non-spherical kinetic shapes, rather than thermodynamically favored spherical shapes. While the asphericity is not ideal, the particles are still quite usable as they still have a low aspect ratio and have magnetic properties that approximate those of spheres. Particle size distribution histograms (Figure 2.16) for the large scale reaction show both nanoparticles in the supernatant and the magnetic nanoparticle agglomerates agree well with the SAXS data. Both analyses suggest the scale-up reaction may have lost some control when it comes to shapes of the particles, but the average particle size remained constant. The data discussed here shows that a large scale synthesis yields useful iron nanoparticles, displaying this method is viable for the industrial setting. Further experimentation may be desirable to refine and better understand the eccentricites involved in the large scale reaction to get more uniform particles.

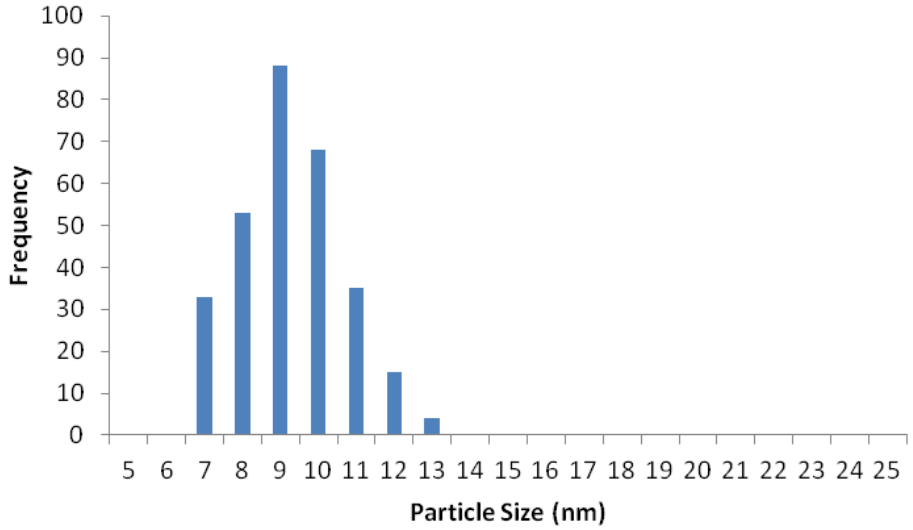

(a) Histogram of size distribution of the nanoparticle supernatant from the scale-up reaction synthesis.

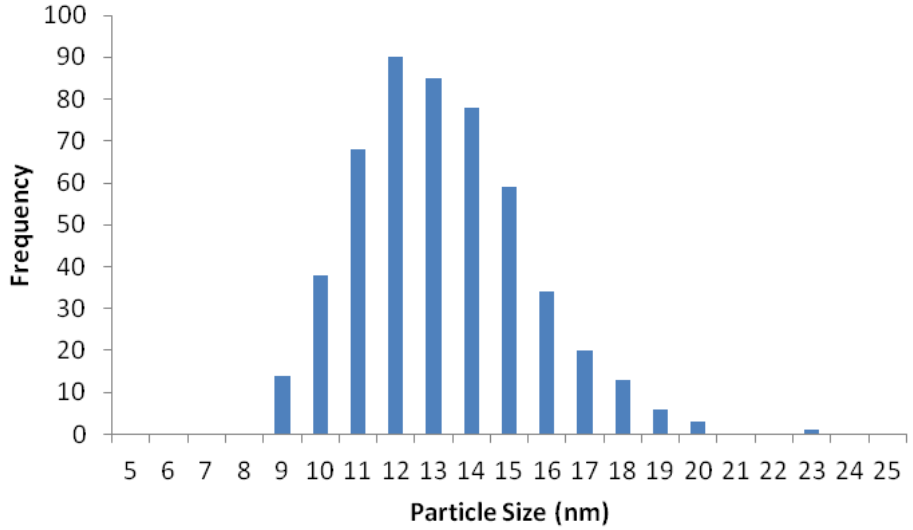

(b) Histogram of size distribution of the nanoparticle magnetic agglomeration from the scale-up reaction synthesis.

Figure 2.16: Histograms of particle size distribution of (a) the supernatant, and (b) the magnetic agglomerates of the scale up reaction synthesis.

2.5 Conclusions

Liquid phase thermal decomposition, combined with careful air-free techniques and carefully chosen reaction conditions, enabled some tuning of size, shape, and particle dispersity. Dodecylamine kept the particles from agglomerating without oxidizing the surface of the particles. The data shows that the use of un-purified, off the shelf chemicals was sufficient to synthesize particles in the size range we desired.

The nanoparticles synthesized were characterized by TGA, DC Magnetometry (through a SQUID Magnetometer), SAXS, and TEM. The TGA analysis gave us a baseline for the synthesized particles in order to characterize further reactions such as the ligand exchange and composite work as will be discussed in chapters 3 and 4.

The magnetometry data showed the particles were still blocked at all temperatures analyzed up to 300 K and still exhibit some hysteresis at room temperature. The remnant magnetic moment found by the field sweep on the SQUID was an order of magnitude lower than that of bulk iron, and would disappear altogether at temperatures above the blocking temperature.

The data acquired by SAXS were analyzed and converted from magnetite to zero-valent particle diameters, to show that the small scale synthesis produced roughly 12.4 nm particles with 20% dispersity. The large scale reaction synthesized approximately 10 nm particles with 29% dispersity,

which is larger due to the difficulty of controlling parameters of such a large scale reaction.

All of the TEM images taken were analyzed to measure average particle size. Results for the supernatant of the small scale synthesis showed an average particle size of 8 nm and the magnetically separated particles synthesized were 13 nm. The large scale reaction generally agreed, with an average of 9 nm particles in the supernatant and 13 nm particles in the magnetically separated particles. All four experimental average ranges agreed well with the SAXS data. The average values of the small scale synthesis and the large scale supernatant agreed completely, but the large scale magnetically precipitated particles were measured to be 2-3 nm's larger than the SAXS data.

One of the reasons for this discrepancy could be the aspherical non-uniformity of the larger scale synthesis magnetically agglomerated particles. The difference in shape could have skewed the measurement data slightly. The SAXS data was fit to a spherical model, so the asphericity was largely ignored and the particles were fit to some average diameter. The TEM diameters, on the other hand, had the Feret diameter measured (also known as the caliper diameter) which is the largest distance between two points on the surface of the particle. The ferret diameter will therefore overstate the diameter of any aspherical particle.

The comparison of the two scales of reaction show that the method is sound for the synthesis of roughly 9 to 13 nm particles and that the dispersity and size tuneability become more difficult to control as the initial reagent volumes increase. This fact is noteworthy especially when applying this synthesis to industrial uses where even larger reaction volumes will be employed. The conclusions made in this chapter show that these particles would be useful for further reaction and characterization as a material for use in transformer cores.

CHAPTER 3- SURFACE CHEMISTRY AND LIGAND EXCHANGE

3.1 Introduction

Surface chemistry is vital to the success of the many applications of nanoparticles. The surface area of a nanoparticle is very large in comparison to its mass[52] that leads to a greater reactivity than larger (micron-sized and above) particles.[53, 54] The surface coatings of nanoparticles are also crucial to determining their properties,[55, 56] in particular, their stability and solubility.[12] The chemistry at the surface of the particles can also control the distance between particles, either in solution or in a composite.

Surfactants prevent nanoparticles from fusing to each other as they are formed. Dodecylamine was used as the surfactant for the synthesis of zero-valent iron nanoparticles (Figure 3.1). This long chain amine was used because studies have shown a direct relationship between the formation of an oxidation layer on the surface of the particles and the chemistry of the surfactant.[12, 33] For example alcohols or carboxylic acids can oxidize the surface of iron particles.

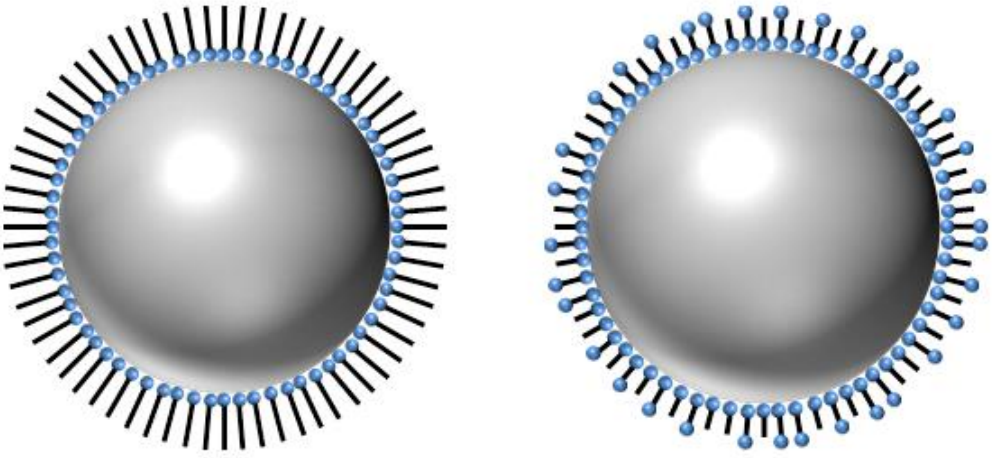

(a) (b)

Figure 3.1: Scale drawings of 12 nm iron nanoparticles with surfactants bound to the surface, where (a) represents the original surfactant (dodecylamine), and (b) represents the exchanged ligands, hexyl amine and 1,6-diaminohexane.

Another consideration when choosing a surfactant is how well it binds to the surface of the nanoparticles. For some applications, ligands attached to particle surfaces need to be exchangeable for reactivity reasons.[57] In this research, the long-chain amine surfactant was exchanged with a mixture of a shorter chain amine and diamine (Figure 3.1). This exchange yields reactive sites at the ends of the diamine straight chain alkyls attached to some proportion of the particles surface. This amine reactivity is important since it will allow the particles to be reactive with epoxides and create a cross-linked nanocomposite without the addition of an accelerator (as would be common in commercial epoxy systems). More about the epoxide and matrix-free

chemistry will be presented in the next chapter. This chapter details the chemistry and characterization of the ligand exchange for the nanoparticles.

Another important aspect of the exchange ligands are their sizes. The hexyl chains are approximately half the length of the dodecyl chains, so assuming equal numbers of molecules per particle, the shorter chains halve the amount of organic material bound to the particles. This is an important consideration for a material where the goal is to minimize the organic content. Shorter chain amines are not practical as they become increasingly volatile. Hexylamine was chosen as the best compromise between small size, low volatility, and cost. Both hexylamine and 1,6-diaminohexane are inexpensive, commodity chemicals.

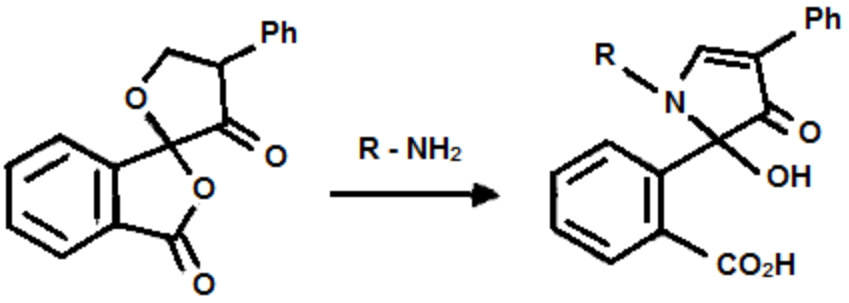

Figure 3.2: Chemical structure and pathway of reactivity for fluorescamine, used for fluorescence tagging of iron nanoparticle ligands.

Fluorescence tagging was used to quantify the presence of reactive amines on the surface of the particles. The specific fluorescent tag chosen was fluorescamine (Figure 3.2). Fluorescamine is a spiro compound that is not

fluorescent, but reacts with primary amines to form easily detectable and strongly fluorescent products. The UV-Vis absorbance of fluorescamine has peaks at 235, 276, 284, and 306 nm. Fluorescamine represents a convenient qualitative tag for reactive amines on the surface of the particles, with the appearance of fluorescence signaling their presence. UV-vis spectroscopy can then be used to quantify the amount of fluorescamine bound to the particles. The experimental details and data for the ligand exchange and qualification via fluorescamine are described in this chapter.

The intended use for these functional nanoparticles is to react with a multi-functional epoxide to form a hardened epoxy nanocomposite. In a traditional 2-part epoxy system, the amine functional nanoparticles would be referred to as the hardener and one of the primary properties reported would be the amine equivalent mass. Simply stated, the amine equivalent mass is the mass of hardener divided by the number of active amines contained in it. For a pure, single component material this would be the molecular weight divided by the number of amines per molecule. For polymers or mixtures, where there is not a single molecular weight, nor a single number of amines per molecule, this represents an average. Calculating the amine equivalent mass of these iron nanoparticles in the same manner as any other epoxy hardener will provide the necessary information to form a well-cured, stoichiometrically balanced, epoxy nanocomposite. All of the necessary information to perform

this calculation is presented in the analyses described here and this calculation will be performed near the end of the chapter.

3.2 Experimental

3.2.1 Methods and Materials

All of the experiments in this section were prepared in a nitrogen atmosphere glovebox (MBraun) to keep the reactions air- and water-free. All of the reagents used in these experiments were purified and distilled before being brought into the glovebox and were stored in the same environment.

Amines can be harmful to the recirculation purifier catalyst of a nitrogen glovebox.[58] The amines can bind to the surface of the copper(0) oxygen scavenger. Copper-nitrogen complexes do not efficiently regenerate into copper metal during the standard regeneration at high temperature with a hydrogen gas purge. Special considerations were necessary for working with these reagents in the glovebox. No volatile amines were stored in the glovebox in their pure form. All volatile amines were purified, made into solutions of no higher than 10% concentration and then parafilmed and stored in a freezer within the glove box. It was then necessary to let the reagent warm and fully melt before use, to ensure appropriate concentrations of the aliquots removed.

3.2.2 Preparation of Amine Mixture Solution for Ligand Exchange

The short chain amines, hexylamine and 1,6-diaminohexane, were chosen for this ligand exchange they are long enough to provide some colloidal stability, while also allowing for crosslinking in later reactions.

The hexylamine was distilled (through a vacuum transfer process)[58] before it was brought into the glovebox. Ten milliliters of hexylamine was added to a round bottom flask under a nitrogen atmosphere and frozen with liquid nitrogen. After the liquid was completely frozen, the flask was put under vacuum for 15 minutes. The hexylamine underwent two freeze-thaw cycles or until the hexylamine no longer bubbled upon melting. Once degassed, the hexylamine was frozen once more and connected to another evacuated round bottom flask. This two flask system was evacuated and the liquid nitrogen cooling bath was moved from the hexylamine to the empty flask. A bulb-to-bulb distillation and the purified hexylamine was warmed under nitrogen, sealed, and brought into the glovebox.

The purified, neat hexylamine was diluted immediately with hexane to form a 10% solution. This sample was sealed, and stored in the glovebox freezer. Working in the glove box with the circulation purifier turned off whenever amines were being used became common practice. After each use of amines in the glove box, the system was purged with nitrogen for at least 15 minutes, in order to ensure all of the volatilized amines were removed from the glovebox prior to turning the circulation purifier back on.

1, 6- diaminohexane is a solid at room temperature and was purchased purified and under inert atmosphere. A 100 g container was purchased from Sigma-Aldrich and brought directly into the glovebox for use. A 10% solution in hexane was made and stored in the glovebox freezer.

Experiments were done to determine the optimum ratio of monoamine to diamine for use in the particle ligand exchange reaction. It was discovered that 100% diamine made the nanoparticles agglomerate and crash out of solution preventing further reaction. This is attributed to the bi-functional molecules binding to more than one particle, causing wholesale agglomeration. The behavior caused by bi-functional surfactants is known in the literature.[59] A 50 / 50 ratio of monoamine to diamine was found to work well, allowing for reactivity while also keeping the nanoparticles from sticking together and precipitating out of solution.

The order of addition of the reagents was also found to have an effect on the final reactivity of the ligand exchanged particles. Exchange of the longer amine for the shorter amines was relatively fast with equilibrium being reached within a few minutes. This quick exchange led to the conclusion that the monoamine and diamine needed to be mixed together as a solution before being added to the nanoparticles. If the diamine was added first, the reactivity of the particles changed, with more of the particles reacting with each other rather than the secondly added monoamine. Therefore, the two amines were first mixed, in equal parts, in a separate vial and then added to

the particles for reaction. This resulted in a 5% weight by volume solution of each, hexylamine and 1,6-diaminohexane, being added to the nanoparticles.

3.2.3 Reaction of Amine Mixture with Zero-Valent Iron Nanoparticles

The 10% monoamine and diamine solutions were added, in equal parts, by volume, to a vial to create a 5% mixture. A 750 µL aliquot of this mixture was added to a 750 µLs of nanoparticles and vortex mixed for 2 minutes. The reaction was then placed on a stirrer and allowed to come to equilibrium for an additional 2 hours.

The nanoparticles were pulled down to the bottom of the reaction solution using a strong permanent magnet on the outside of the reaction vial. The excess amines were decanted from the reaction vial and the nanoparticles were washed with 1 mL of hexane and vortexed for 2 minutes. The magnetic collection, decanting, and washing process was performed 3 times. This process ensured the removal of all excess amines. The ligand exchanged nanoparticles were stored in the glovebox in a minimal volume of hexane for characterization and further reaction.

3.2.4 Amine Mediated Fluorescent Tagging

Fluorescamine is unique in that it only fluoresces after it has been reacted with a primary amine.[60] This allowed for immediate confirmation of the reactivity of the ligand exchanged nanoparticles through the use of a handheld UV lamp.

A solution of fluorescamine was made up with 25 mg of fluorescamine in 5 mL of dry THF. A 0.5 mL aliquot of ligand exchanged iron nanoparticles (concentration 5 mg/mL) was put into a vial with 200 µL of fluorescamine solution and allowed to stir and react overnight. When the reaction was stopped, the particles were pulled down with a strong permanent magnet and the excess fluorescamine solution was decanted from the vial. The particles were washed three times with 1 mL of hexane. These nanoparticles were diluted to 1 mL total volume in hexane and observed for fluorescence under a UV Lamp (Figure 3.4). Fluorescence after excess fluorescamine is washed from the solution confirms the presence of primary amines bound to the particles that were free to react with the fluorescamine molecules. The solution was then analyzed by UV-Vis spectroscopy.

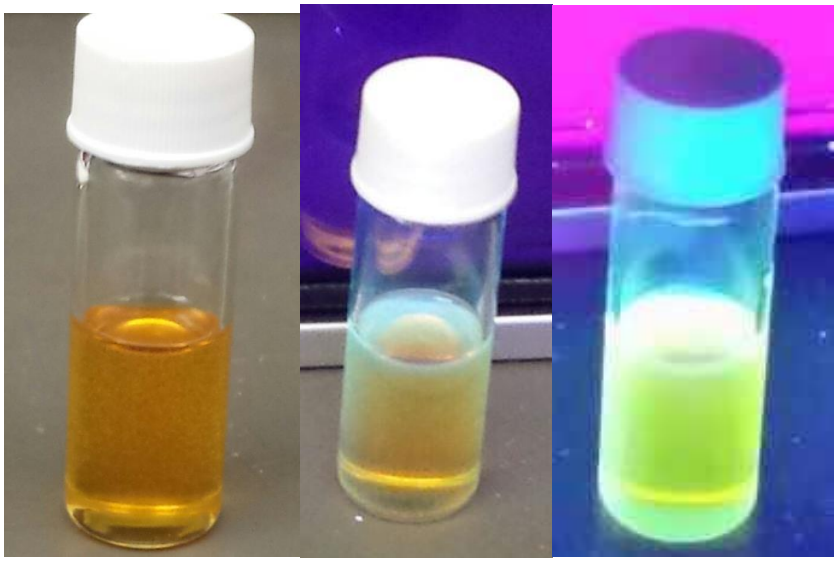

Figure 3.3: Fluorescence of Fluorescamine Reacted Ligand Exchanged Zero-Valent Iron Nanoparticles. Left: White light, no UV light. Center: White light, UV light on. Right: No white light, UV light on.

3.3 Results and Discussion

3.3.1 UV-Vis Spectroscopy

A Cary 6000i UV-Vis-NIR Spectrophotometer was used to characterize the ligand exchange reactions. The spectrometer has a dual beam which allows for simultaneous analysis of a blank and sample. The instrument was calibrated at the time of use at both 0 and 100% absorption each time a sample was analyzed in order to minimize drift, or variability, in measurements due to the sample housings.

The graph presented in Figure 3.5, shows the absorbance of fluorescamine at 306, 284, 276, and 235 nm. These absorption peaks, along with the visual fluorescence, confirm the presence and availability of amine functional groups on the nanoparticle surfaces. Unlike fluorescence measurements, the UV-vis absorptions are linear with concentration, which will allow the calculation of the concentration of reacted fluorescamine in the sample. This will be important to determine the amine equivalent mass that is described below.

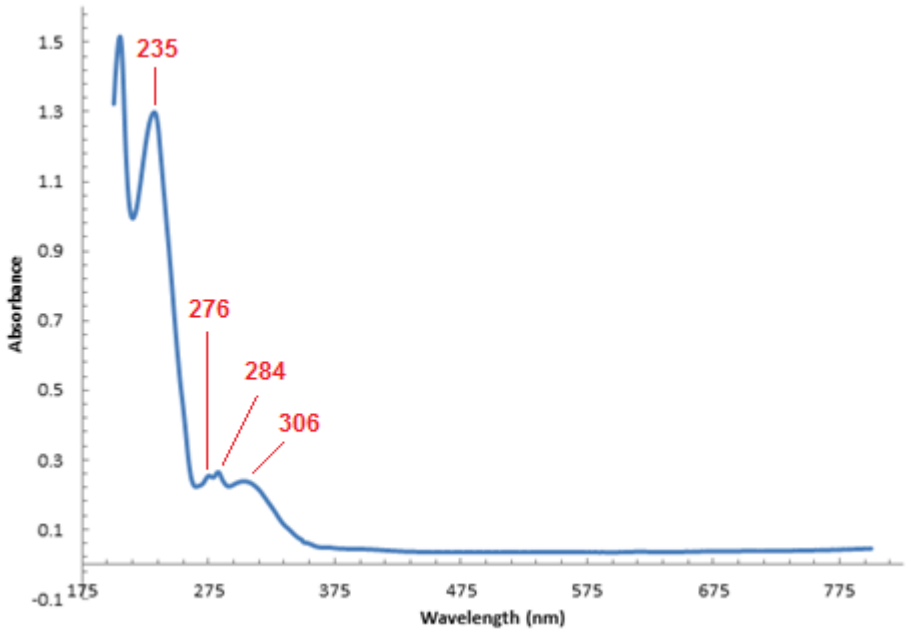

Figure 3.4: UV-Vis Spectra of Fluorescamine coated ligand exchanged zero-valent iron nanoparticles.

3.3.2 Thermo Gravimetric Analysis (TGA)

A portion of the ligand exchanged iron nanoparticles were separated into a tared weigh boat and analyzed by TGA, ramped up to 600 ºC at 10 ºC per minute and held at 600 ºC for 45 minutes. Both TGA and DSC data were recorded. The TGA results are shown in Figure 3.6 and Table 3.1 below.

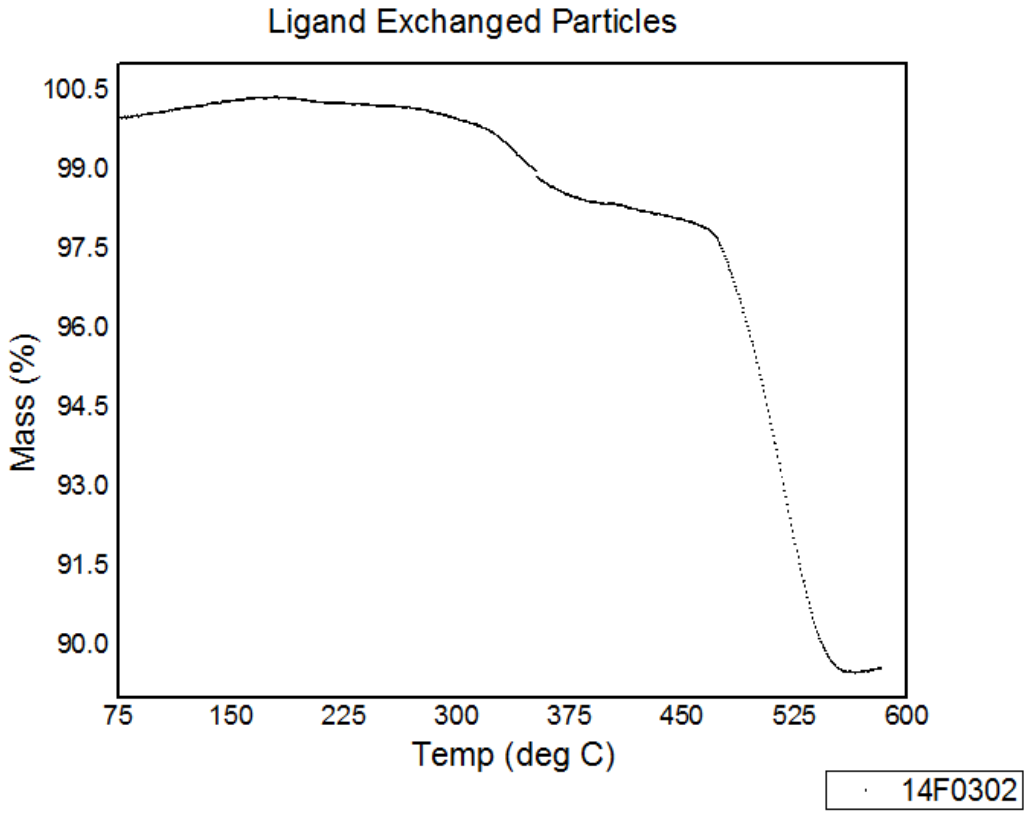

Figure 3.5: TGA Results of Ligand Exchanged Zero-Valent Iron Nanoparticles.

Table 3.1: Ligand Exchanged Nanoparticle Mass Loss by TGA

Sample	Initial Weight	Final Weight	Mass Loss	Percent Loss
Total Ligand	6.69 mg	6.00 mg	0.69 mg	10.33%
Diamine	6.58 mg	6.00 mg	0.58 mg	8.724%

The total loss of mass in the sample is due to both of the amines attached to the surface of the nanoparticles. In these experiments, two separate mass losses can be seen at different temperatures, corresponding to the two separate boiling points of the hexylamine and 1,6-diaminohexane. Since it is

only the diamine that gives reactivity to the surface of the nanoparticles and the boiling point of the diamine is higher than that of the monoamine, it is the second mass loss that is of importance for quantitatively determining how many reactive diamines are attached to the nanoparticle surfaces. This second mass loss gave an 8.724% loss or 0.584 mg of the 1,6-diaminohexane for the ligand exchanged reaction. When calculating the amount of epoxide needed to form a well-cured epoxy with the iron nanoparticles, an estimate of the amount of diamine present on the nanoparticles is required. The above calculation will therefore be used as an estimator for the epoxide reactions in the subsequent chapter.

3.3.2 Calculation of the Amine Equivalent Mass

To calculate the amine equivalent mass requires determination of the number of reactive amines in a sample of known mass. The reaction of fluorescamine with primary amines is extremely well-studied and is essentially quantitative under normal circumstances.[60] On the surface of a particle, there may be issues with steric hindrance in amines that are adjacent on the surface. This, however, will be an issue with any surface-bound chemistry, so the fluorescamine reaction represents a valid approach to determining the content of reactive amines (though not necessarily the total number of amines).

The data required for this calculation was collected in the UV-vis analysis of the fluorescamine functionalized particles. This data, in numerical form, is

presented in Table 3.1. Amine-reacted fluorescamine has four strong UV-vis absorptions with known extinction coefficients. Values of fluorescamine concentration using all four absorbances are shown in Table 3.1. They agree with each other within a few percent, with the exception of the value determined from the 235 nm absorption. This peak appears in a crowded regime of the UV-vis spectrum where a number of other functional groups can interfere, including the 185 nm absorption of alkyl amines.[61] For further calculations, the 235 nm absorbance is ignored and the concentration is determined from the averages of the other absorbances.

Table 3.2: UV-vis Spectroscopy of Amine-Reacted Fluorescamine

Peak Position	Peak Height [Absorbance]	Extinction Coefficient [M^{-1}]	Molarity
306 nm	0.221	3800	5.81×10^{-5}
284 nm	0.244	4100	5.94×10^{-5}
276 nm	0.238	3900	6.10×10^{-5}
235 nm	1.242	25900	4.79×10^{-5}

Tabular data from the spectrum shown in Figure 3.5. Molarity of amine-reacted fluorescamine is calculated from the known extinction coefficients.

If we take reactivity with fluorescamine to be the definition of a reactive amine; then the concentration of amine-reacted fluorescamine is equal to the concentration of the reactive amines. The measured concentration of reactive amines is 6.0×10^{-5} M. This concentration was for a 1 mL solution containing 2.5 mg of iron nanoparticles. Dividing the number of moles of amine in the 1 mL sample (6.0×10^{-8}) by the number of grams of the iron nanoparticle sample (2.5×10^{-3}) yields the amine equivalent mass of 42,000 g/mole. This is

much larger than is typical for epoxy hardeners which are generally in the 10's or 100's of g/mole. This is because hardeners are generally polymers with repeat units that contain amines, where the number of repeat units is small to keep the viscosity low. The small amine equivalent mass is necessary to get a well-cured material when the hardener molecule is so small. In this case the hardener unit is an iron nanoparticle with a full complement of surfactants on the surface, a much more massive unit.

It is worth performing a few more calculations to understand the nature of the hardener unit that has been created. A 12 nm iron particle with the bulk density of iron would weigh approximately 4.3×10^6 g/mole. Adding 10% to account for the mass of the organic ligand, as determined by TGA, brings the final mass to 4.7×10^6 g/mole. Dividing this calculated mass of an iron nanoparticle by the amine equivalent mass previously determined yields an average of about 112 reactive amines per iron nanoparticle. So, despite the unusually high amine equivalent mass, the nanoparticle hardener has an enormous degree of functionality.

3.4 Conclusions

Through the various characterization methods described above, it is apparent the ligand exchange, from a long chain monoamine on the surface of the nanoparticles to a mixture of a shorter chain monoamine and diamine, has occurred to a measureable extent. The exchange allowed for the addition of reactive amine sites, 112 on average per particle, to the surfaces of the

nanoparticles. This high degree of functionality will drive its behavior as a hardener which will be required for use of these particles in the creation of a matrix-free nanocomposite system as will be discussed in the next chapter.

Chapter 4- Matrix-Free Nanocomposite Formation

4.1 Introduction

Because the material we are synthesizing is interesting because of its possible application for use in transformer cores, we decided to set a goal to create a scale model of a magnetic toroid. The scale model would be made of a matrix-free iron nanocomposite which would have low loss and high magnetic saturation. To achieve that goal we first had to figure out the processing steps required to create an epoxy filled with iron particles at a high volume to weight ratio. This includes optimizing the distribution and curing conditions.

The first system attempted was made with commercial epoxy procured from Sigma-Aldrich and micron-sized iron powder. The next system was made by encapsulating magnetite, Fe_3O_4, nanoparticles into the same commercial epoxy. Processing issues arose with this system including separation and settling of the particles in the epoxy while curing. Also, removal of the solvent into which the particles were dispersed in prior to mixing with the epoxy proved difficult. The problem of uneven particle dispersion into a matrix is a common one that is understood at a practical and theoretical level.[62] This inability to produce uniform nanocomposites using this approach led us to quickly abandon this method, and no iron nanocomposites were made from these materials.

The decision was made to use a custom epoxy system that could better encapsulate and uniformly disperse the nanoparticles into a matrix. Matrix-free composites utilize the surface reactivity of nanoparticles to chemically bind particles to one another with a uniform spacing that is solely dependent on the functionalization of the nanoparticle surfaces. Here, the use of a diamine created primary amine reactive sites at the ends of the ligands attached to the nanoparticle surfaces. By taking advantage of this reactivity, a matrix-free composite was formed through the addition of an epoxide in a stoichiometric ratio to the diamine. The resulting product would be a matrix-free nanocomposite composed of uniformly spaced iron nanoparticles.

4.2 Experimental

4.2.1 Methods and Materials

The extreme sensitivity of the iron nanoparticles requires care when processing them into a composite. The synthesis and ligand exchange of the zero-valent iron nanoparticles are performed in strictly an air- and water-free environment. Epoxides however, are often undesirable in a nitrogen glove box environment due to the active oxygen and its potential for reacting with air-sensitive species. The inability to perform the final steps in an inert atmosphere meant that the particles needed to be added to the encapsulant in air. The mixing of the particles into the epoxide, therefore, needed to be done as quickly as possible to keep the particles from oxidizing. Once cured,

epoxies are well-known for their oxygen barrier properties[63] and the prevention of oxidation of the iron nanoparticles.

Gas bubbles trapped inside cured epoxies create structural instabilities that can result in increased brittleness and cracking, as well as giving inhomogeneous magnetic properties. In order to keep the matrix-free nanocomposite system as uniform as possible, the epoxy/particle mixture was degassed both before, and during, curing. Degassing occurs via a vacuum oven set at the curing temperature of the epoxy to remove gas bubbles throughout the curing process. The nanoparticle-epoxide solution is put into the oven under vacuum, removing any gas bubbles from the solution as it is heated. The sample is cured under vacuum at 60 ºC for a minimum of four hours.

4.2.2 Addition of Carbonyl Iron Powder to a Sigma-Aldrich Epoxy System

The Sigma-Aldrich epoxy system used consists of four parts: epoxy embedding medium, 2-dodecenylsuccinic anhydride (DDSA), Methyl-5-norbornene-2,3-dicarboxylic anhydride (methylnadic anhydride or NMA), and 2,4,6-tris(dimethylaminomethyl)phenol (DPM-30), an accelerator. To create a cured epoxy, the four parts above are mixed together in specific ratios as provided by the manufacturer. Five milliliters of the final epoxy mixture was added to a vial along with 100 µL of the accelerator and 26.738 g of micron sized iron powder. A 1/10th scale toroid model mold was printed for use in this application using a 3D printer. The plastic mold was sprayed with mold

release and filled with the epoxy/particle mixture. The mold was put into the vacuum oven at 45 ºC over the weekend to cure as the structural stability of the plastic mold was only rated to 50 ºC, hence, the lower temperature. The model toroid made (Figure 4.1) was loaded to 40% by volume (82% by mass).

Figure 4.1: A 1/10th scale model toroid casting of iron particles 40 vol.% in custom epoxy formulation.

Removal of the cured epoxy from the plastic mold proved impossible. The cured epoxy bonded to the polar surface of the acrylate plastic even though mold release was used. The scale model had dimensions such that little structural stability was inherent to the mold that made the ring brittle and more likely to crack or break. These deficiencies forced the development of a flexible mold made of silicon. The silicon mold proved to be easier to work

with, bending while being removed instead of breaking the mold or the encapsulated particles. Part of the sample was analyzed by AC Magnetometry.

4.2.3 Addition of Amine Terminated Iron Nanoparticles to a Sigma-Aldrich Epoxy System

The third system was made by the addition of ligand exchanged iron nanoparticles to the Sigma-Aldrich commercial epoxy system. Two milliliters of the epoxy were added to a vial along with 40 µL accelerator, and 500 µL iron nanoparticles. The epoxy was mixed and poured into two sample vials for AC and DC Magnetometry analyses, respectively. Sample vials were placed inside the vacuum oven, degassed, and cured over the weekend at 45 ºC. Due to problems with dispersion and the ‘popping’ effect of the solvent in the vacuum oven, the samples were spattered into the oven while curing and could not be analyzed by magnetometry. The processing issues prevented further efforts with this system.

4.2.3 Reaction of Amine Terminated Iron Nanoparticles with Epichlorohydrin, a Monoepoxide

The monoepoxide, epichlorohydrin, was added to the ligand exchanged iron nanoparticles for proof of concept. If the particles were functionalized as expected, the epoxide would react and increase the mass loss seen by TGA as compared to previous analyses. To a vial, 500 µL ligand exchanged

nanoparticles were added to 127.2 µL of epichlorohydrin (a 50:1 ratio of epoxide to nanoparticles). This reaction was done outside of the nitrogen glove box. The sample was mixed, in a sealed vial, on a shaker plate for 2 hours to allow the reaction to complete. A strong permanent magnet was used to pull the particles out of solution to the bottom of the sample vial, and the excess epoxide was decanted. The monoepoxide reacted particles were washed three times with 1 mL hexane. The sample was transferred to an aluminum weigh boat and analyzed by TGA.

4.2.4 Reaction of Amine Terminated Iron Nanoparticles with N,N-Diglycidyl-4-glycidyloxyaniline, a Triepoxide

Approximately 90 mg of ligand exchanged nanoparticles were washed and stored in a minimal volume of hexane. A calculation was done to find the stoichiometric amount of triepoxide, N,N-Diglycidyl-4-glycidyloxyaniline, needed to react with the nanoparticles to get a 3:1 ratio and fully cross-link the nanoparticles with the epoxide. To the nanoparticles, 5.11 µL of N,N-Diglycidyl-4-glycidyloxyaniline were added and the vial was vortex mixed for 2 minutes. The new volume was transferred into two separate aluminum weigh boats and put inside the vacuum oven to degas. After cycling vacuum twice in a 60 ºC oven, the mixture was allowed to cure for three hours. The resultant mixture appeared to be dry and brittle, and as the triepoxide is not volatile, this suggested the reaction had taken place. One sample was

transferred into a tared aluminum weigh boat and analyzed by TGA. The second sample was analyzed by AC Magnetometry.

4.3 Results and Discussion

4.3.1 Thermo Gravimetric Analysis (TGA)

A sample (~15 mg) of the monoepoxide modified nanoparticles was loaded into a tared weigh boat and analyzed by TGA. The resulting graph (Figure 4.2) was used to calculate the amount of monoepoxide that reacted with the primary amines on the surface of the nanoparticles. Several individual mass losses can be seen in the TGA graph, but they appear to significantly overlap that makes it difficult to assign the losses to the specific species in the sample.

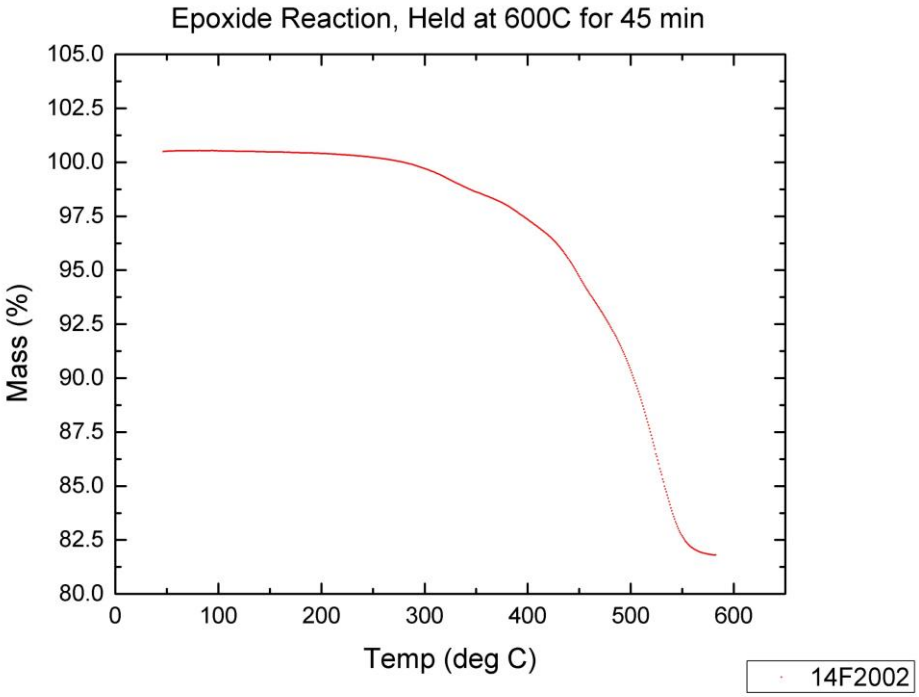

Figure 4.2: TGA of Monoepoxide

From the calculations made in chapter 3, for the percent loss of sample due to the ligand exchange amines of ~10%, we can attempt to calculate the loss of the current sample that is due to the monoepoxide molecules attached to the primary amines on the surface of the nanoparticles.

Table 4.1: Monoepoxide Reacted Nanoparticle Mass Loss by TGA

Sample	Initial Weight	Final Weight	Mass Loss	Percent Loss
Amines	15.476 mg	13.900 mg	1.576 mg	~10%
Monoepoxide	13.900 mg	12.660 mg	1.24 mg	8.19%

Table 4.1 shows that ~8.2% loss in the sample is expected to be from the monoepoxide. If we assumed a 1:1 reaction of primary amine to monoepoxide, a 100% yield would net ~1.56 mg of 1,6-diaminohexane in the sample. 1.56 mg of 1,6-diaminohexane would represent almost 100% of the mass loss attributed to both of the amines on the surface of the particles. It isn't possible that the particles are coated with 100% diamine, as that causes immediate and unmistakable agglomeration of the nanoparticles. Polar solvents are known to be capable of displacing surfactants from metal surfaces and pulling them into solution.[64] So, a plausible explanation is that the large excess of epichlorohydrin acted as an aggressive solvent, removing some of the bound amines from the surface. This would significantly increase the amount of reactive amines present and would lead to an excess of reacted monoepoxide. Future reactions were performed at approximately stoichiometric ratios to prevent this complication.

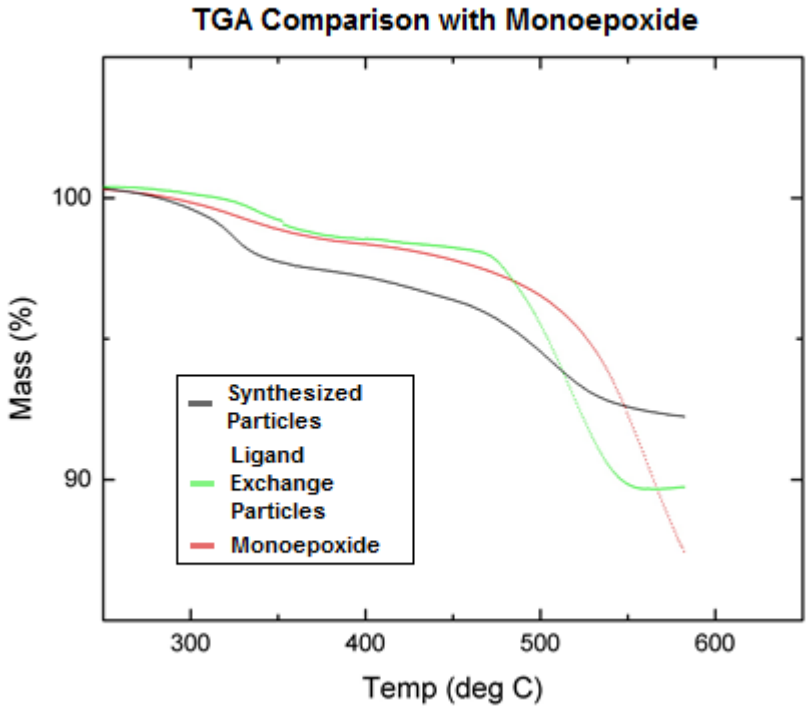

Figure 4.3: Comparison of synthesized particles, the ligand exchanged particles and the monoepoxide reacted nanoparticles.

Comparing the normalized TGA graphs of the three samples analyzed to this point: synthesized particles, ligand exchanged particles and particles that have been reacted with a monoepoxide; shows the mass loss differences between the samples clearly. Figure 4.3 shows the increase in loss of mass from the samples as continued reactions are done on the particles. This is a qualitative way to show the reactivity of the particles after ligand exchange. This proof of concept led to the use of a triepoxide for cross-linking the particles into a matrix-free nanocomposite.

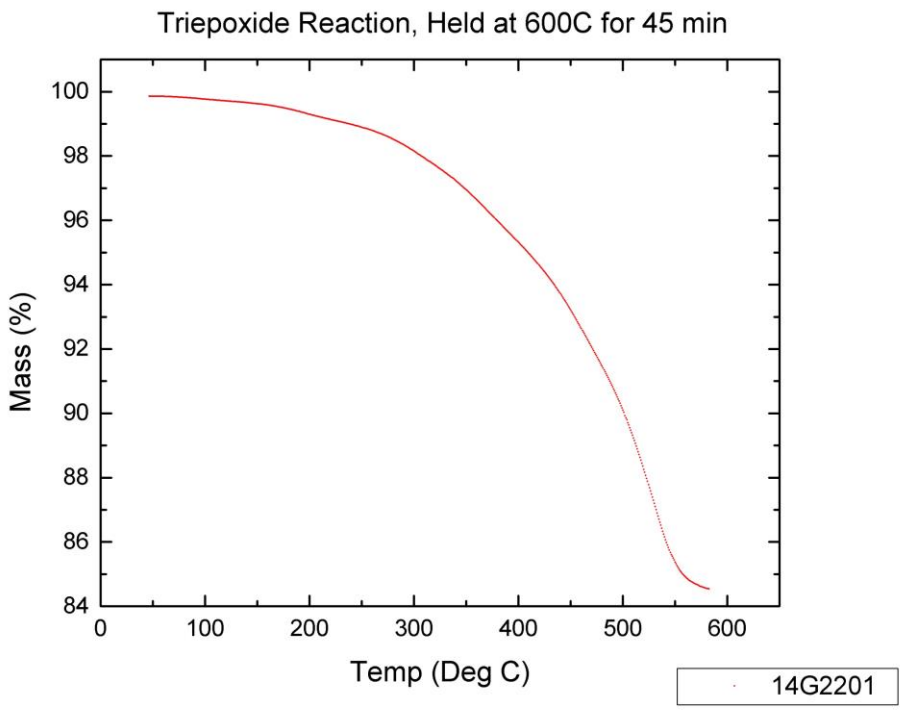

Figure 4.4: TGA of Triepoxide

Figure 4.4 shows the TGA analysis of ligand exchanged iron nanoparticles that were reacted with a triepoxide, N,N-digylcidyl-4-glycidoxyaniline, ($C_{15}H_{19}NO_4$). The total mass loss of the sample is given in Table 4.2. Using the same assumption as for the monoepoxide reaction of ~10% loss of mass from the two amine ligands on the particle surfaces, we have ~5.5% loss from the triepoxide. Due to the more complicated steric restrictions involved with a tridentate epoxide, a direct calculation of the number, or percentage, of diamines on the surface of the particles is not possible. The mass loss was associated to the amine ligands and the triepoxide on the surface of the nanoparticles and the sample was dry and hardened. These facts allow us to

safely say that the epoxide cross-linked the nanoparticles to a measureable extent.

Table 4.2: Triepoxide Reacted Nanoparticle Mass Loss by TGA

Sample	Initial Weight	Final Weight	Mass Loss	Percent Loss
Epoxy and Amines	36.306 mg	30.693 mg	5.613 mg	15.46%

One of the goals of this research was to create a nanocomposite with maximum loading by volume of particles to the total volume. The loading percentage for the triepoxide reaction detailed here is ~38% by volume (Table 4.3).

Table 4.3 Percent Loading, Particles to Composite

Mass Iron	Mass Remaining	Volume Iron	Total Volume	Weight % / vol.
30.693 mg	5.613 mg	0.0039 mL	0.0103 mL	37.86%

Graphing all of the TGA analyses in one figure (Figure 4.5) allows us to see the differences in the reactions upon addition of each new component. The triepoxide reaction clearly shows the mass loss of a single component (only one smooth curve throughout the temperature range). This confirms that the particles were cross-linked into a nanocomposite, creating one solid matrix.

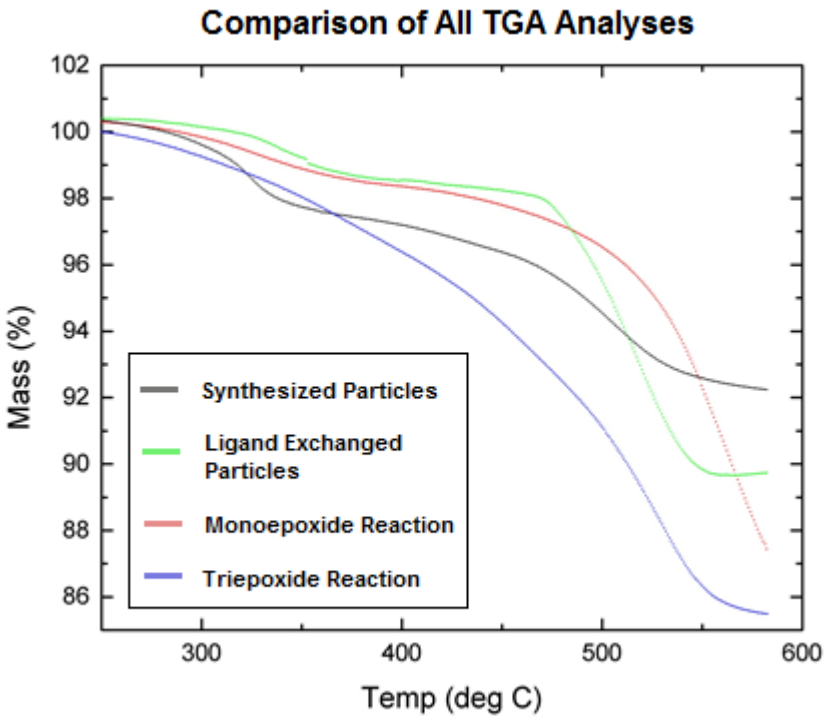

Figure 4.5: Comparison of synthesized particles, ligand exchanged particles, monoepoxide reacted particles, and triepoxide reacted particles.

Lastly, for comparison purposes, a sample of the cured Sigma-Aldrich epoxy system was analyzed by TGA (Figure 4.6). The TGA curve of a typical epoxy can help illuminate similarities with our unconventional composite system, allowing for another qualitative confirmation of a cured matrix system.

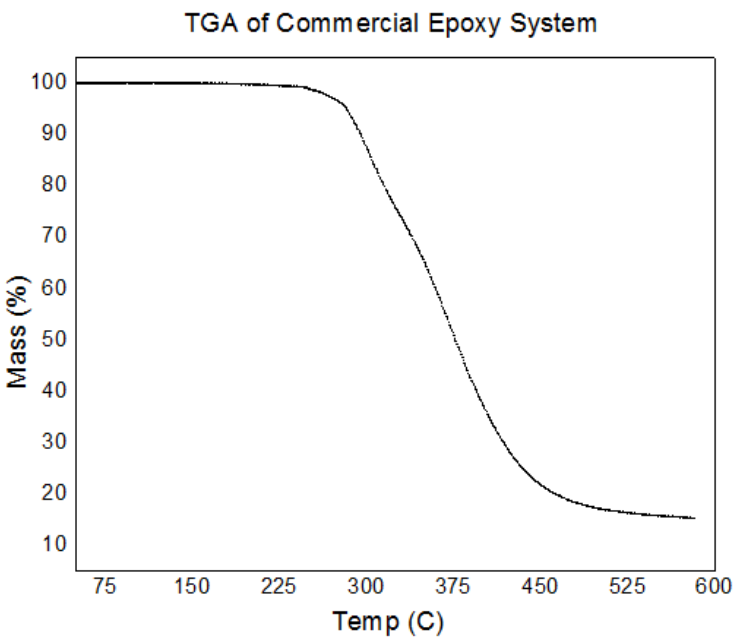

Figure 4.6: Commercial Epoxy System.

Table 4.3: Commercial Epoxy Mass Loss by TGA

Sample	Initial Weight	Final Weight	Mass Loss	Percent Loss
Sigma Aldrich Epoxy	81.564 mg	12.532 mg	69.031 mg	84.64%

The commercial epoxy TGA curve is similar to that seen with the triepoxide reaction; a single curve with steady mass loss. As the commercial epoxy system contains different components than the triepoxide, with no iron, the percent loss of material is much greater (Table 4.3).

4.3.2 AC Magnetometry

All AC magnetometry data was taken on an IMEGO: DynoMag AC Susceptometer (Figure 4.7). The DynoMag is a portable magnetic instrument capable of measuring the AC susceptibility of liquids, powders, and solid samples. The frequency range is from 5 Hz up to 200 kHz, with a resolution in magnetic moment in the range of 3.10^{-11} A·m^2, and excitation amplitude of 0.5 mT.

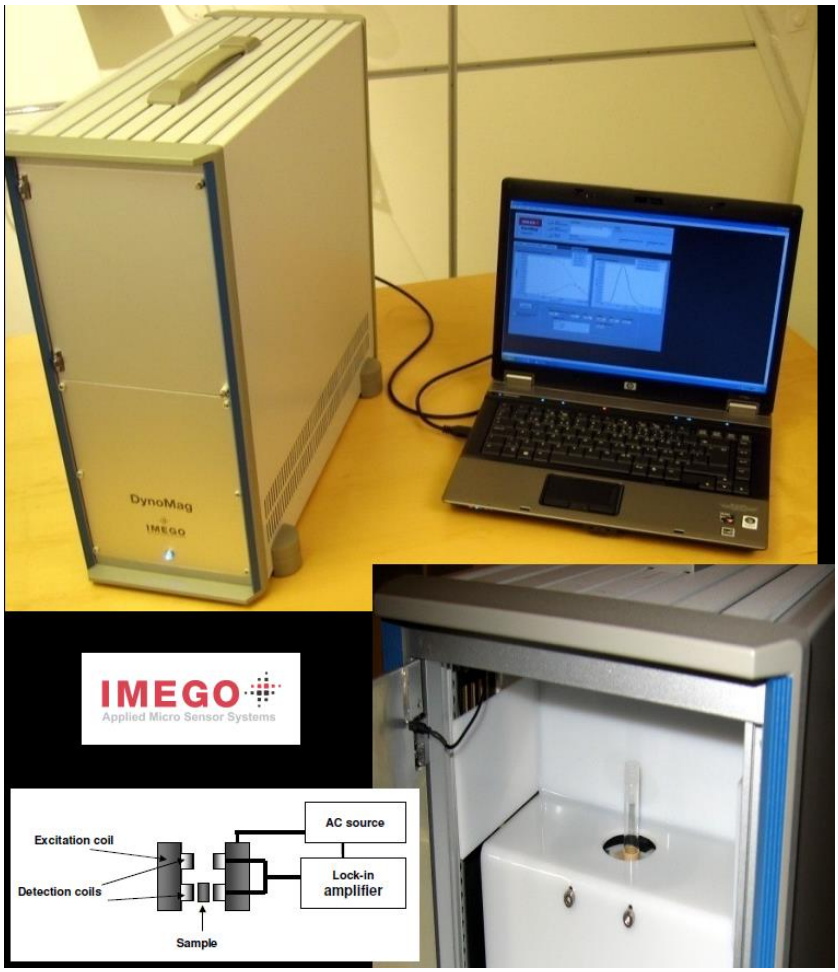

Figure 4.7: DynoMag AC Susceptometer, sample introduction, and coil

Three types of samples were measured using AC Suceptometry: MetGlas (an amorphous iron alloy used commercially in transformer applications), a micron-sized iron powder composite, and matrix-free zero-valent iron nanocomposites (Figure 4.8). All had essentially flat susceptibility for frequencies up to 10 kHz, when the Metglas susceptibility began to fall off as frequency increased. The micron-scale iron composite began to fall off next near 50 kHz, while the nanocomposites material showed a more gradual decrease at high frequencies. As the frequency increases, it becomes more difficult for the magnetic moments in the material to keep up with the change in magnetic field. The lag behind the magnetic moment shows up on the graph as a drop in the susceptibility (Figure 4.8).

The nanocomposite out-performed the other materials, showing its potential for use as an improved material in transformer core applications where fast switching is important. What this frequency dependent relative susceptibility does not show is that the nanocomposites material begins with a much higher susceptibility, and therefore maintains a higher susceptibility than the other materials at all frequencies. This can be discerned from the DC magnetometry in the next section.

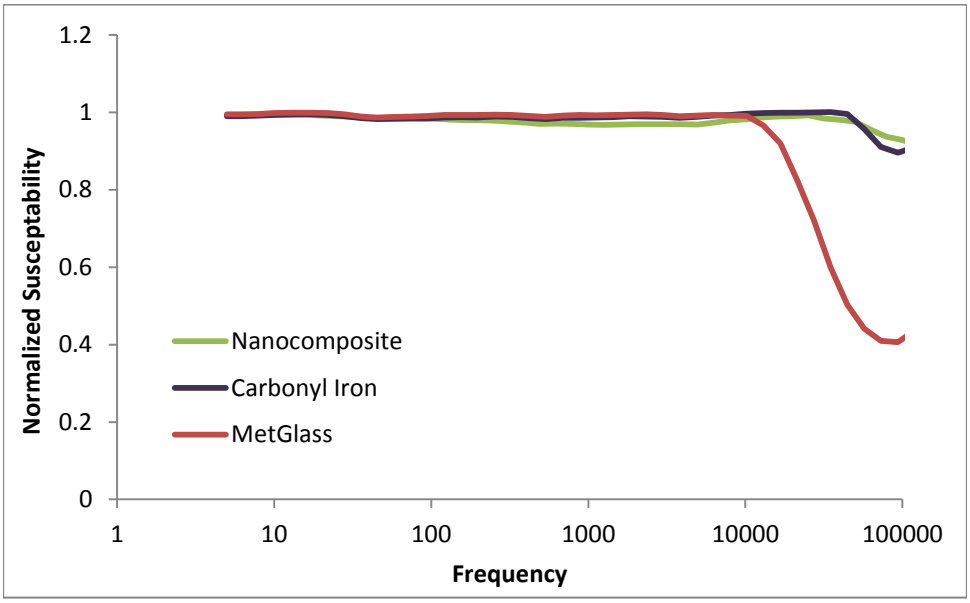

Figure 4.8: Comparison of micron sized powder iron composite, Metglas, and our matrix-free nanocomposite. The ability of the material to perform under higher frequencies increases with the materials listed, with the nanocomposite performing the best.

4.3.3 SQUID DC Magnetometry Data

For comparison purposes, the sample containing micron sized carbonyl iron powder and the commercial epoxy system from Sigma-Aldrich was analyzed by performing a field sweep on the DC SQUID magnetometer (Figure 4.9). Since the micron sized iron particles have no interesting temperature dependent behavior, a temperature sweep was not performed on this sample.

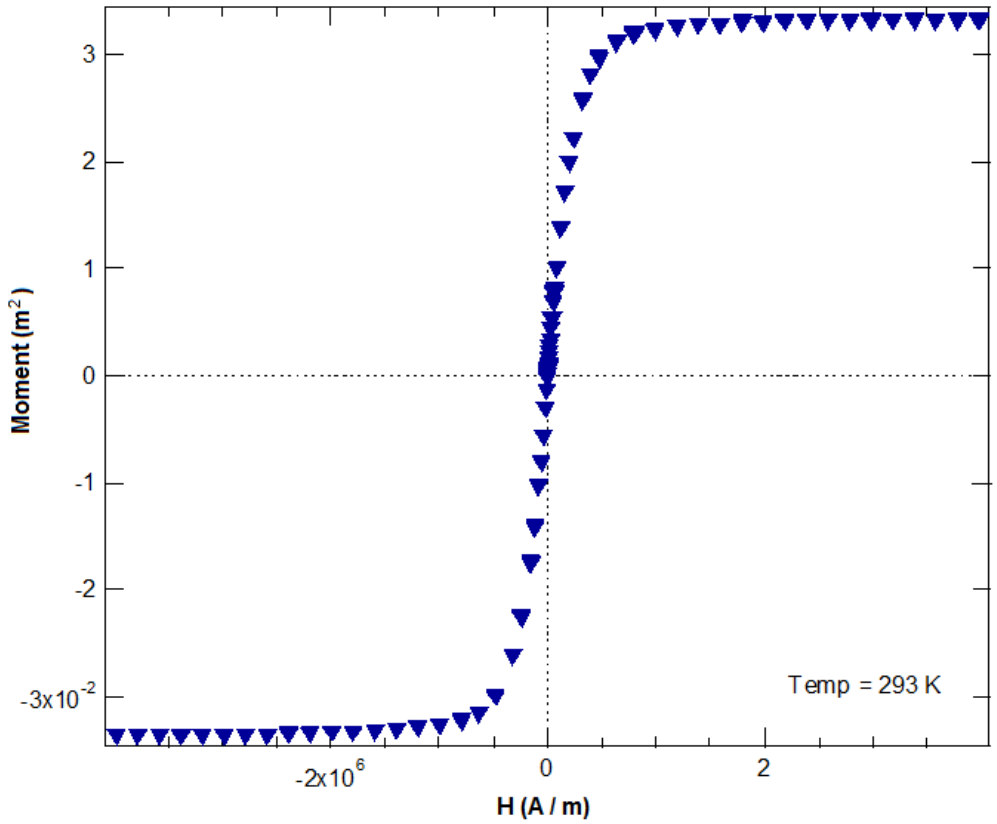

Figure 4.9: DC SQUID Magnetometry Field Sweep Data. Field Range -5 T to 5 T. Maximum magnetic moment: 3.33×10^{-2} A·m^2.

The triepoxide reaction was also analyzed by DC Magnetometry. From the data obtained (Figure 4.10), a clear blocking transition is seen at 350 K. The discontinuity at 220 K, however, is most likely a physical effect of the organic material, such as a glass transition temperature of the epoxy. Typical glass transitions for epoxides are around 60 ºC, though this is not a typical. The ratio of nanoparticles to epoxide was not optimized for this sample of nanoparticles; the final product was slightly rubbery at room temperature

rather than fully cured. In all likelihood, this phenomenon occurred due to an excess of epoxide in the sample.

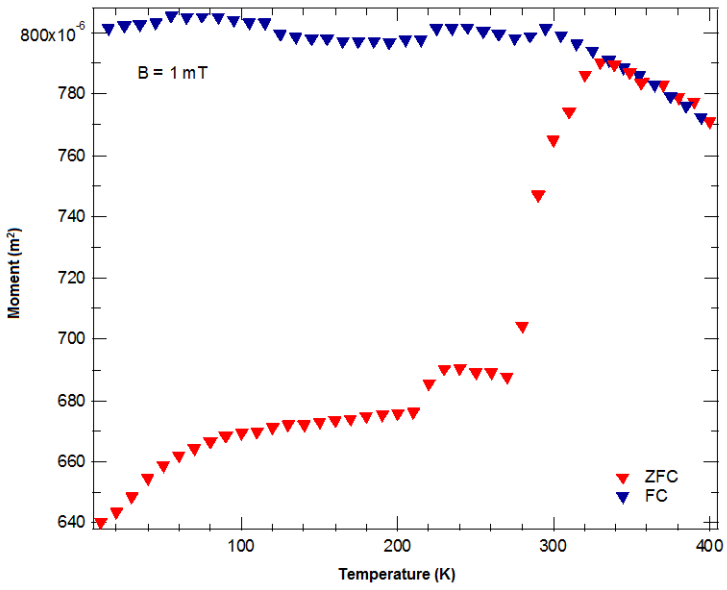

(a)

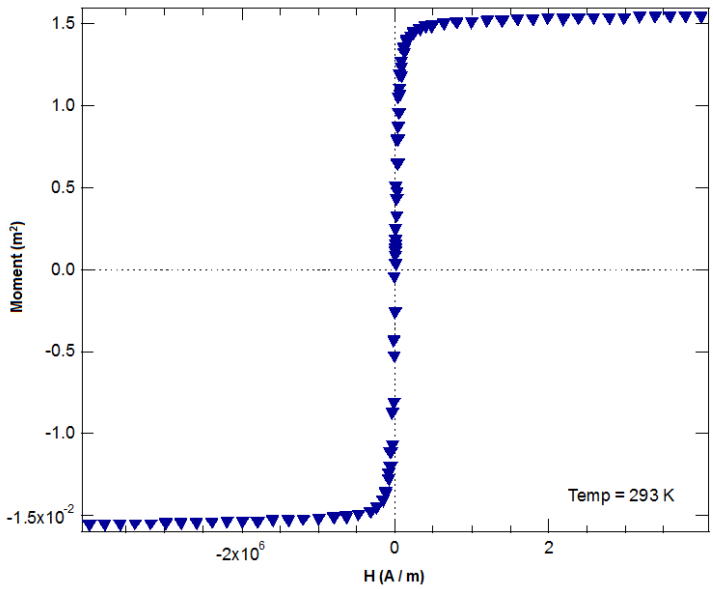

(b)

Figure 4.10: SQUID Data for Triepoxide Reacted Zero-Valent Iron Nanoparticles. (a) ZFC / FC magnetization curves for nanoparticles with an applied field of 1 mT, temperature range of 10 K to 400 K. Blocking Temperature is 340 K. (b) Magnetization curve of particles at 250K Field sweep from -5T to 5 T. Maximum magnetic moment is 1.55×10^{-2} $A \cdot m^2$.

The graph in Figure 4.10(a) shows that there is no hysteresis above 350 K, but that the sample is hysteretic below that temperature. This suggests that 350 K is a blocking transition and not a physical transition like all of the others described in chapter 2. It also tells us this material would be ideal for applications that work above ambient temperatures, near 350 K.

For a well-dispersed sample of nanoparticles, we expected to detect a blocking temperature just above 300 K. This appears to have shifted to a higher temperature due to the formation of the composite. The nanocomposite is at 80% loading by mass and the temperature shift is less than 50 K, (~30 K). Therefore, for room temp applications of the nanocomposite, particles that block ~30 K below room temperature, before dispersion into the nanocomposite, would be required. This would allow the nanoparticles to shift to higher temperatures in the nanocomposite and yet still block at room temperature.

The shift to higher blocking temperatures is likely due to interparticle interactions. When close enough together, neighboring particles can feel each other's fields. This interaction causes the particle's magnetic moments to take more thermal energy to realign due to the additional magnetic anisotropy in the environment. The nanoparticles behave as slightly larger particles than they are when interacting with other particles. Interacting particles usually have broader transitions than non-interacting particles. As seen in Figure 4.9, broad transitions are not present.

The broad transition phenomenon is generally seen because interacting particles in a typical sample have interparticle distances that vary widely. This leads to a vast variety of environments and a broadening of the transition on the graph. Matrix-free nanocomposites are different due to the nearly identical particle-particle distances in the sample. The uniformity of environment would therefore lead to a shifted blocking temperature of a constant amount.

Finally, one interesting direct comparison can be made between the two composite materials. The nanoparticles have a different mechanism of alignment with the magnetic field that would be expected to yield a higher susceptibility than multi-domain particles (see Chapter 1 for details). The approach to saturation for these samples is shown in Figure 4.11. The plot clearly demonstrates the higher susceptibility of the nanocomposites material and the faster magnetization that it produces.

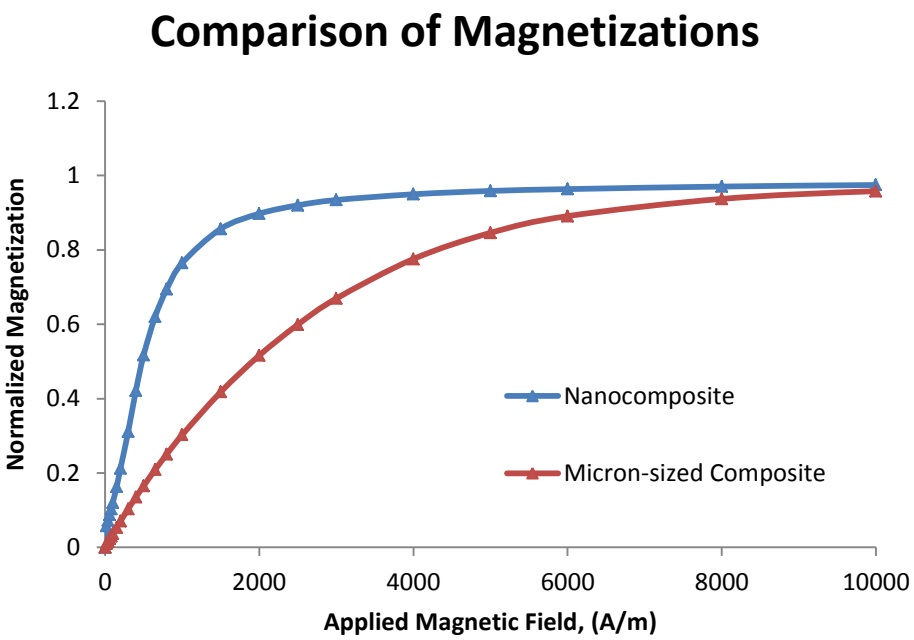

Figure 4.11: Comparison of the magnetization of the nanocomposite to a micron-scale composite. The nanocomposite has significantly higher magnetization at lower fields, and a faster approach to saturation.

For example, the nanocomposite is at more than 50% of its saturation value with an applied field of 500 A/m. For the micron scale composite to reach this same 50% value, approximately 2000 A/m is required. Since most applications do not achieve full saturation of the material, this faster approach to saturation is an important advantage of the nanocomposite material.

4.4 Conclusions

The addition of a triepoxide, N,N-glycidyl-4-diglycidoxyaniline, to ligand exchanged iron nanoparticles under vacuum at 60 ºC overnight, created a

matrix-free nanocomposite which was characterized by TGA and AC and DC Magnetometry. The results of these characterizations showed a low loss material of ~38% by volume loading (80% by mass), which has extremely high susceptibility. The blocking temperature of this nanocomposite was 350 K, slightly above room temperature.

This nanocomposite material was shown to be unique in several important ways. Due to the presence of a blocking temperature, we know that the iron nanoparticles in the material are superparamagnetic above 350 K, and therefore have no hysteresis above that temperature. As hysteresis is one of the main forms of loss in magnetic materials, the lack thereof allows this material to be a more efficient magnetic material. The second largest form of magnetic loss is in the form of eddy currents, which are also absent from nanoparticles in a non-conducting matrix. The nanocomposite performs better in a high frequency magnetic field than other conventional materials tested, as shown by AC magnetometry, and has a narrow transition as shown by DC magnetometry. These two characteristics show that the spacing between the particles is uniform and the interactions between the particles are small.

CHAPTER 5- SUMMARY AND CONCLUSIONS

The principle objectives of this thesis were 1) to design a synthetic method to create zero-valent iron nanoparticles of uniform size over a range in which the particles exhibit superparamagnetic properties, 2) to chemically change the reactivity at the surface of the nanoparticles through a ligand exchange, and 3) to encapsulate the reactive nanoparticles into a matrix-free nanocomposite that would be useful as a material in the application of transformer cores. These goals were achieved through the use of a novel method using unpurified reagents at a larger scale than ever reported in literature previously. The achievements in each chapter are summarized here.

5.1 Synthesis of Zero-Valent Iron Nanoparticles

The synthesis method demonstrated in this study conclusively formed zero-valent iron nanoparticles from the decomposition of $Fe(CO)_5$ in dioctylether as shown through SAXS and TEM measurements. This work described a novel method for producing zero-valent iron nanoparticles using unpurified reagents on a larger scale than any previous work in unoxidized iron nanoparticles. Spherical, approximately 12 nm particles, with 25% size dispersity were synthesized using this method. Further, it was demonstrated for this system that while control of shape becomes more difficult as scale is increased, the size and dispersity are still appropriate for use in most applications.

5.2 Surface Chemistry and Ligand Exchange

Through the use of fluorescence tagging and UV-vis Spectroscopy, we have concluded that the surfactant used in the synthesis of the zero-valent iron nanoparticles can be sufficiently exchanged with shorter chain amine ligands. The mixture of a monoamine and diamine of the same length create reactive primary amine sites on the surface of the nanoparticles while also keeping the nanoparticles sufficiently separated, avoiding agglomeration. The ligand exchange was done to create reactive sites for cross-linking the nanoparticles together in a matrix. For the 12-13 nm zero-valent iron nanoparticles synthesized in the first chapter, the average number of reactive amines is 112 per particle. This allows for the reactive amines on the surface of the nanoparticles to act as a nanoparticle hardener with an enormous degree of functionality.

5.3 Matrix-Free Nanocomposite Formation

By reaction of the ligand exchanged zero-valent iron nanoparticles with a triepoxide, we were able to successfully create a matrix-free nanocomposite with high susceptibility and low loss as seen by DC magnetometry. Through the use of AC magnetometry, we were able to determine the matrix-free nanocomposite performed better in a high frequency magnetic field than other, more conventional materials. The results of the DC magnetometry showed that the particles in the nanocomposite unblock at 350 K, behaving

superparamagnetically above this temperature. This material would be ideal for use in applications that are slightly above room temperature.

The results presented here represent a substantial improvement over current materials used in transformer core applications. The zero-valent iron nanoparticles synthesized show no hysteresis above 350 K and therefore do not exhibit hysteresis loss. The second major form of magnetic loss, eddy current interactions, is reduced by the fact that the nanoparticles are uniformly spaced within the matrix-free composite and therefore do not show significant conduction. The methods presented here produce rather large quantities of zero-valent iron nanoparticles, 16 g in one particular large scale reaction, which is a yield of over 70% for the synthesis reaction.

5.4 Ongoing and Future Work

The synthesis method used in this thesis is amenable to optimization and fine tuning beyond the scope of the work presented here, to increase scale further and also improve the product yield. Further fine tuning of size, shape and dispersion are also possible.

Equally as important as the synthesis of the nanoparticles, is the modification of the particle surfaces that create the functionality required for cross-linking nanoparticles into a matrix-free composite. Investigation into the use of other, similar ligands, with properties that may increase the functionality or reactivity of the nanoparticle surfaces may be worthy.

Further optimization of the structural properties of the nanocomposite can be done to tune the properties for specific applications. The use of different epoxides, with more or less epoxide reactivity, would change the specific magnetic properties of the material through changes in density and dispersion of the nanoparticles in the nanocomposite.

REFERENCES

1. DOE, *Benefits of Using Mobile Transformer and Mobile Substations for Rapidly Restoring Electrical Service*, 2006. p. 1-48.
2. Kappenman, J., *Geomagnetic Storms and Their Impacts on the U.S. Power Grid*, M. Corporation, Editor 2010, Oak Ridge National Laboratory. p. 1-197.
3. *Report of the Commission to Assess the Threat to the United States from Electromagnetic Pulse (EMP) Attack*, 2008. p. 1-208.
4. *Large Power Transformers and the U.S. Electric Grid*, 2012. p. 1-55.
5. Analysts, G.I., *Solar Panels: A Global Strategic Business Report*, 2011. p. 761.
6. Dixon, L.H.J., *Eddy Current Losses in Transformer Windings and Circuit Wiring.*
7. Usov, N.A., *Low frequency hysteresis loops of superparamagnetic nanoparticles with uniaxial anisotropy.* Journal of Applied Physics, 2010. **107**(12): p. 123909.
8. Raikher, Y.L. and V.I. Stepanov, *Dynamic hysteresis of a superparamagnetic nanoparticle at low-to-intermediate frequencies.* Journal of Magnetism and Magnetic Materials, 2006. **300**(1): p. e311-e314.
9. Fairbairn, W., *Iron: Its History, Properties, and Processes of Manufacture*. 1861: A. and C. Black.
10. Alfe D., K.G., Gilian M.J., *Structure and dynamics of liquid iron under Earth's core conditions.* Physical Review B, 2000. **61**(1): p. 11.
11. Lide, D.R., *CRC Handbook of Chemistry and Physics*. Vol. Internet Version. 2005, Boca Raton, FL: CRC Press. 2660.
12. Huber, D.L., *Synthesis, properties, and applications of iron nanoparticles.* Small, 2005. **1**(5): p. 482-501.
13. Mathon, O., et al., *Dynamics of the Magnetic and Structural a-e Phase Transition in Iron.* Physical Review Letters, 2004. **93**(25): p. 255503.
14. Misawa, T., K. Hashimoto, and S. Shimodaira, *The mechanism of formation of iron oxide and oxyhydroxides in aqueous solutions at room temperature.* Corrosion Science, 1974. **14**(2): p. 131-149.
15. *Standard Terminology Relating to Nanotechnology*, in *ASTM Standard E2456*2012, ASTM International: West Conshohocken, PA. p. 4.
16. Angelo P. C., S.R., *Powder Metallurgy: Science, Technology and Applications*. 2009, New Delhi: PHI Learning Private Limited.

17. Magnetics, *A Critical Comparison of Ferrites with Other Magnetic Materials*, 2000, Magnetics: Division of Spang & Company: Butler, PA.

18. Brunsman, E.M., et al., *Magnetic properties of monodomain Nd-Fe-B-C nanoparticles.* Journal of Applied Physics, 1996. **79**(8): p. 5293-5295.

19. Issa, B., et al., *Magnetic nanoparticles: surface effects and properties related to biomedicine applications.* Int J Mol Sci, 2013. **14**(11): p. 21266-305.

20. Laurent, S., et al., *Magnetic Iron Oxide Nanoparticles: Synthesis, Stabilization, Vectorization, Physicochemical Characterizations, and Biological Applications.* Chemical Reviews, 2008. **108**(6): p. 2064-2110.

21. Gubin, S.P., et al., *Magnetic nanoparticles: preparation, structure and properties.* Russian Chemical Reviews, 2005. **74**(6): p. 489-520.

22. James W. Robinson, E.M.S.F., George M. Frame II *Undergraduate Instrumental Analysis*. 2004, New York: CRC Press. 1079.

23. Yeomans, J.A., *Ductile particle ceramic matrix composites—Scientific curiosities or engineering materials?* Journal of the European Ceramic Society, 2008. **28**(7): p. 1543-1550.

24. Singh, V. and V. Banerjee, *Ferromagnetism, hysteresis and enhanced heat dissipation in assemblies of superparamagnetic nanoparticles.* Journal of Applied Physics, 2012. **112**(11): p. 114912.

25. Moon, T.S., *Domain states in fine particle magnetite and titanomagnetite.* Journal of Geophysical Research, 1991. **96**(B6): p. 9909.

26. Alex Hubert, R.S., *Magnetic Domains: The Analysis of Magnetic Microstructures*. 2009, Heidelberg: Springer.

27. Huber, D.L., et al., *Synthesis of highly magnetic iron nanoparticles suitable for field structuring using a β-diketone surfactant.* Journal of Magnetism and Magnetic Materials, 2004. **278**(3): p. 311-316.

28. Monson, T.C., et al., *Implication of Ligand Choice on Surface Properties, Crystal Structure, and Magnetic Properties of Iron Nanoparticles.* Particle & Particle Systems Characterization, 2013. **30**(3): p. 258-265.

29. Roy, R., R.A. Roy, and D.M. Roy, *Alternative perspectives on "quasi-crystallinity": Non-uniformity and nanocomposites.* Materials Letters, 1986. **4**(8-9): p. 323-328.

30. Roy, R., *Synthesizing new materials to specification.* Solid State Ionics, 1989. **32-33**: p. 3-22.

31. Dach, B.I., et al., *Cross-Linked "Matrix-Free" Nanocomposites from Reactive Polymer−Silica Hybrid Nanoparticles.* Macromolecules, 2010. **43**(16): p. 6549-6552.

32. Ajayan, P.M.S.L.S.B.P.V., *Nanocomposite science and technology*. 2003, Weinheim: Wiley-VCH.

33. Farrell, D., S.A. Majetich, and J.P. Wilcoxon, *Preparation and characterization of monodisperse Fe nanoparticles.* Journal of Physical Chemistry B, 2003. **107**(40): p. 11022-11030.

34. Burke, N.A.D., H.D.H. Stöver, and F.P. Dawson, *Magnetic Nanocomposites: Preparation and Characterization of Polymer-Coated Iron Nanoparticles.* Chemistry of Materials, 2002. **14**(11): p. 4752-4761.

35. G. Katabya, Y.K., A. Ulmanb, I. Felnerc, A. Gedanken, *Blocking temperatures of amorphous iron nanoparticles coated by various surfactants.* Applied Surface Science 2002. **201**: p. 5.

36. Wu, W., Q. He, and C. Jiang, *Magnetic iron oxide nanoparticles: synthesis and surface functionalization strategies.* Nanoscale Res Lett, 2008. **3**(11): p. 397-415.

37. L., K., et al., *Study of magnetic relaxation in partially oxidized nanocrystalline iron*. Vol. 52. 2002, Heidelberg, ALLEMAGNE: Springer.

38. Zhang, D., et al., *Encapsulated iron, cobalt and nickel nanocrystals; Effect of coating material (Mg, MgF2) on magnetic properties.* Nanostructured Materials, 1999. **12**(5–8): p. 1053-1058.

39. K. Suslick, M.F., T. Hyeon, *Sonochemical Synthesis of Iron Colloids.* Journal of the American Chemical Society, 1996. **118**(47): p. 11960-11961.

40. Mohaddes-Ardabili, L., et al., *Self-assembled single-crystal ferromagnetic iron nanowires formed by decomposition.* Nat Mater, 2004. **3**(8): p. 533-8.

41. Smith, T. and D. Wychick, *Colloidal Iron Dispersions Prepared Via the Polymer-Catalyzed Decomposition of Iron Pentacarbonyl.* Journal of Physical Chemistry, 1980. **84**(12): p. 1621-1629.

42. Baev, A.K., I.L. Gaidym, and V.V. Demyanchuk, *Thermal-Decomposition Kinetics of Iron Nonacarbonyl.* Zhurnal Fizicheskoi Khimii, 1975. **49**(10): p. 2575-2577.

43. Huber, D., *Magnetic Agglomeration Method for Size Control in the Synthesis of Magnetic Nanoparticles*, S. Corporation, Editor 2011: USA.

44. Lacroix, L.M., et al., *Stable single-crystalline body centered cubic fe nanoparticles.* Nano Letters, 2011. **11**(4): p. 1641-5.

45. Plicht G., B.M., Brown G., Schillak H., Edwards R., *N2-Nitrogen On-Site Generation for Metal Furnace Atmospheres.* Air Products and Chemicals, Inc., 2002(Rev 2): p. 15.

46. Peng, S., et al., *Synthesis and stabilization of monodisperse Fe nanoparticles.* J Am Chem Soc, 2006. **128**(33): p. 10676-7.

47. Kura, H., M. Takahashi, and T. Ogawa, *Synthesis of Monodisperse Iron Nanoparticles with a High Saturation Magnetization Using an Fe(CO)x-Oleylamine Reacted Precursor.* Journal of Physical Chemistry C, 2010. **114**(13): p. 5835-5839.

48. Fogler, H.S., *Elements of Chemical Reaction Engineering*. Prentice Hall International Series in the Physical and Chemical Engineering Sciences, ed. N.R. Amundson. Vol. 3rd Edition. 1999, Upper Saddle River, NJ 0745: Prentice Hall PTR. 967.

49. Morrish, A.H., *The Physical Principles of Magnetism*. 2001: Wiley-IEEE Press. 700.

50. Langford, J.I. and A.J.C. Wilson, *Scherrer after sixty years: A survey and some new results in the determination of crystallite size.* Journal of Applied Crystallography, 1978. **11**(2): p. 102-113.

51. Sasaki, A., *Size Distribution Analysis of Nanoparticles Using Small Angle X-Ray Scattering Technique.* 2005.

52. Buzea, C., Pacheco, II, and K. Robbie, *Nanomaterials and nanoparticles: sources and toxicity.* Biointerphases, 2007. **2**(4): p. MR17-71.

53. Gunawan, C., et al., *Cytotoxic Origin of Copper(II) Oxide Nanoparticles: Comparative Studies with Micron-Sized Particles, Leachate, and Metal Salts.* ACS Nano, 2011. **5**(9): p. 7214-7225.

54. Gan, Y. and L. Qiao, *Combustion characteristics of fuel droplets with addition of nano and micron-sized aluminum particles.* Combustion and Flame, 2011. **158**(2): p. 354-368.

55. Sperling, R.A. and W.J. Parak, *Surface modification, functionalization and bioconjugation of colloidal inorganic nanoparticles.* Philos Trans A Math Phys Eng Sci, 2010. **368**(1915): p. 1333-83.

56. Verma, A. and F. Stellacci, *Effect of surface properties on nanoparticle-cell interactions.* Small, 2010. **6**(1): p. 12-21.

57. Benning, C.J., *Plastic Foams: The Physics and Chemistry of Product Performance and Process Technology*. 1969, New York: Wiley-Interscience.

58. Shriver D.F., D.M.A., *The Manipulation of Air-Sensitive Compounds*. 1986, New York: Wiley.

59. Gu, J.-A., et al., *Colorimetric and bare-eye determination of fluoride using gold nanoparticle agglomeration probes.* Microchimica Acta, 2013. **180**(9-10): p. 801-806.

60. Udenfriend, S., et al., *Fluorescamine: A Reagent for Assay of Amino Acids, Peptides, Proteins, and Primary Amines in the Picomole Range.* Science, 1972. **178**(4063): p. 871-872.

61. R. M. Silverstein, G.C.B.a.T.C.M., *Spectrometric identification of organic compounds*. 1992, Chichester: Wiley.

62. Kumar, S.K. and R. Krishnamoorti, *Nanocomposites: structure, phase behavior, and properties.* Annu Rev Chem Biomol Eng, 2010. **1**: p. 37-58.

63. Golden, J.H., M.P. Galla, and L.A. Navarro, *Oxygen barrier compositions and related methods*, 2012, Google Patents.

64. Bain, C.D., J. Evall, and G.M. Whitesides, *Formation of monolayers by the coadsorption of thiols on gold: variation in the head group, tail group, and solvent.* Journal of the American Chemical Society, 1989. **111**(18): p. 7155-7164.